Materials Advances

ROYAL SOCIETY OF CHEMISTRY

REVIEW

View Article Online
View Journal | View Issue

Cite this: *Mater. Adv.*, 2024, 5, 1783

Upconversion as a spear carrier for tuning photovoltaic efficiency

Nikita Chaudhary, Mansi Pahuja and Kaushik Ghosh *

Solar energy constitutes a major share of the total renewable energy produced all over the world. Different types of photovoltaics, including silicon, perovskite, and dye-sensitized solar cells, are being explored to increase the energy-harvesting capability to generate maximum energy from the total solar spectrum. However, the current photovoltaic technology does not utilize a large part of the solar spectrum, mainly the infrared region. The unutilized IR radiation is detrimental to solar-cell performance and gradually degrades the lifespan of the devices due to the severe heating effect. In this aspect, upconversion presents a feasible route for harvesting the unutilized part of solar energy; it converts sub-bandgap photons into photons of higher energy. Upconversion nanoparticles include a host matrix and lanthanides as dopant materials, where the constituents can be tuned to obtain the desired range of upconverted wavelengths. This review discusses the various possibilities of utilizing the upconversion matrix to gain the technological know-how to improve the efficiency of existing solar technologies. The major emphasis is on increasing the efficiency of silicon-based photovoltaic technology.

Received 28th October 2023,
Accepted 25th January 2024

DOI: 10.1039/d3ma00916e

rsc.li/materials-advances

1. Introduction

The ever-growing pressure on non-renewable sources of energy like coal and their fast depletion rates is continuously increasing the need to switch to a sustainable solution for high energy demand.[1] When it comes to renewable sources, the sun or solar energy is one of the most used sources for electricity generation across the world. Only 1.8×10^{14} kW of energy falls on earth out of the total energy emitted by the sun at the rate of 3.8×10^{23} kW per second. Even if only 0.1% of this total solar energy is harvested with only 10% average power conversion efficiency, it would be equivalent to four times the total generating capacity of the world, *i.e.*, about 3000 GW.[2] Solar energy has come a long way since the 7th century B.C. when people started using sunlight to light fires using a magnifying glass, to the discovery of the photovoltaic effect by Edmond Becquerel in 1839,[3] and now the global solar energy market is projected to reach $223.3 billion by 2026.[4] Also, solar power amounts to 3% of the global energy generation making it the third largest renewable energy source for electricity generation after hydropower and wind energy.[5] Owing to this large market share and the growing demand for the renewable energy sector, it is inevitable to tune the efficiency of solar devices to satisfy the needs of the coming generation and its sustainable future.

The most promising technology in the PV industry is crystalline silicon (c-Si) solar cells. The abundance of silicon in the earth's crust (28%), its non-toxic nature, and its relative cost-effectiveness make it a fundamental component in the electronic industry. The very first silicon solar cell was developed by Daryl M. Chapin, Gerald L. Pearson, and Calvin S. Fuller at Bell Laboratories in 1954, having an efficiency of 6%.[6] This technology has reached such spectacular heights that could be realized from the fact that more than 125 GW of c-Si modules were installed in 2020 and a total of 700 GW have been installed to date. A humongous share of 95% of the market is ruled by c-Si solar cells.[7] However, the photovoltaics are bound by the Shockley–Quisser limit (or SQ limit) that gives an upper limit of 32% (theoretically) to the power conversion efficiency due to factors like process-induced interfacial defects as well as limited broadband absorption. The interfacial defects lead to nonradiative recombinations[8,9] and, experimentally, the maximum efficiency has been reported to be 26.81%.[10]

Apart from defect states, another limiting factor that comes into the picture is the overall percentage of the solar spectrum that is being absorbed by the solar cell. The higher energy photons, typically in the UV region, cause thermalization losses whereas photons having energy less than the band gap of silicon are not absorbed by the device, which leads to transmission losses (almost 50% of the overall spectrum).[11–13] Similar issues are also present in the third generation of solar cells including perovskite solar cells and dye-sensitized solar cells (DSSCs). The narrow band gap (approx. 1.8 eV) of the commonly used dyes in DSSCs including N749 and N719 could only harvest sunlight from 300 to 800 nm, skipping a large part of

Institute of Nano Science & Technology, Knowledge City, Sector-81, SAS Nagar, Manauli P.O.-140306, Mohali, Punjab, India. E-mail: kaushik@inst.ac.in

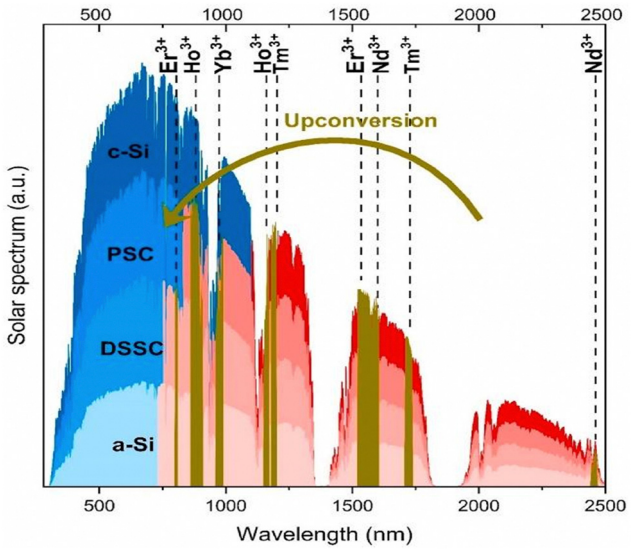

Fig. 1 Parts of the solar spectra of different solar cell types, utilized (in blue) and lost (in red), and the absorption ranges (in brown) of the upconverting Ln^{3+} ions.[11]

the solar spectrum, mainly the infrared and near-infrared region.[14] The most promising perovskite materials also face similar issues that impact their power conversion efficiency. Many perovskite materials, including tin and lead-based perovskites, have a typical band gap range, from 1.2 eV to 1.4 eV leading to narrow solar spectrum absorption.[15] Therefore, a large part of the solar spectrum goes unutilized in most solar cell technology markets.

The losses due to sub-bandgap photons could be reduced using the concept of upconversion (UC), where two or more low-energy photons (IR region) are converted into a single photon having higher energy (visible region) (shown in Fig. 1) *via* a long-lived intermediate state through anti-Stokes emission.[16] The concept of upconversion was first introduced by Dutch-American physicist Nicolas Bloembergen in 1959.[17] In theory, it was predicted that with the help of an ideal upconverter, the standard Air Mass 1.5 global (AM 1.5G) spectrum power conversion efficiency can be tuned up to 50.7% from the basic limit of 32%.[12] This phenomenon finds its applications in various fields, including photovoltaics, bioimaging, sensors, OLEDs, biomedicines, *etc.* This UC concept is similar to the impurity-photovoltaic-effect or IPV, where impurities are introduced in the bulk material, which behave as upconverting materials and provide intermediate energy levels for upconversion.[18] A similar approach is used in an upconversion matrix where rare earth elements with rich 4f energy levels are commonly used to transform lower energy light into visible light and promote solar cell efficiency. This review highlights the various mechanisms of upconversion and how different dopants could render different luminescence spectra. Applications in different types of solar cells, including silicon solar cells, dye-sensitized solar cells, and perovskite solar cells, have also been discussed in detail, along with the UCNPs integration strategies.

2. Upconversion mechanisms and materials

2.1. Mechanisms

The basic mechanisms of upconversion in nanocrystals are excited state absorption (ESA), energy transfer upconversion (ETU), photon avalanche (PA), cooperative sensitization upconversion (CSU), and cross-relaxation (CR), depicted in Fig. 2. In organic molecules, the mechanism of upconversion is triplet–triplet annihilation (TTA).[19–22]

2.1.1. Excited state absorption. An ESA process takes place through an intermediate metastable state. In this process, a low-energy photon is absorbed, and electrons are transferred to the metastable state. Further, a second low-energy photon is absorbed, and the electron is transferred to the higher excited state. When this electron relaxes back to the ground state, a radiative emission of a higher energy photon takes place, which is known as upconversion. This process is not easily observed because of the high population of the intermediate metastable state required for the absorption of the second photon. Thus, a high pumping power source is necessary to observe ESA.[23]

2.1.2. Energy transfer upconversion. The requirement of high pumping power is eliminated in the energy transfer upconversion process, which is relatively easy to achieve. It requires a nanocrystal matrix having two kinds of luminescent centres, which are namely, emitters and sensitizers. The role of a sensitizer is to absorb the lower energy photons and transfer them (radiatively) to emitter centres, whereas upconversion takes place at the emitter centre when the electron is relaxed back to the ground state. However, energy level matching is essential for efficient energy transfer from the sensitizer to the emitter.[24]

2.1.3. Cross-relaxation. Cross-relaxation includes ion–ion interactions where ion 1 in the higher energy state, E_2, relaxes back to the lower energy state E_1. This energy is transferred to another ion (ion 2), which results in excitation from the ground state to the excited state E_1. Here, both ions could be similar or dissimilar. This mechanism is usually exploited for tuning the output of upconversion known as concentration quenching. The efficiency of this mechanism depends on the doping concentration in the nanocrystals.[25]

2.1.4. Cooperative sensitization upconversion. The CSU process includes a three-ion system where two ions are similar and act as a sensitizer. Both ions are excited to the E_1 energy level after absorbing the incident radiation. This cumulative energy is transferred to the third ion, which acts as an emitter. Here, two ions cumulatively transfer energy to the emitter ion, and thus, the process is known as cooperative. This, however, is less efficient than ESA and ETU as the resonance between the photons is less in this process.[26]

2.1.5. Photon avalanche. Photon avalanche is a rather complex system that is usually observed in UC lasers. It includes three non-linear behaviours, namely, transmission, emission, and rise time on the pump power intensity. In this process, a highly populated metastable state is achieved through resonant ESA. Initially, all the ions are present in the ground state. To start the

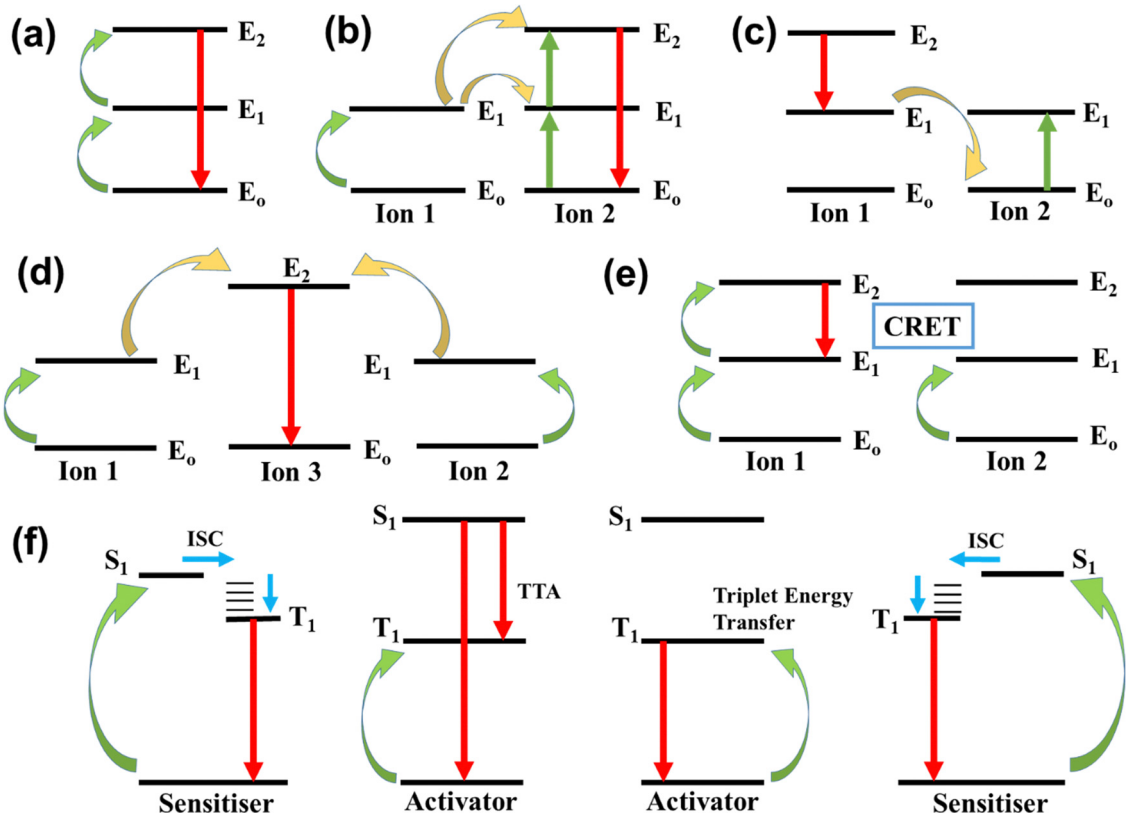

Fig. 2 Schematics of upconversion mechanisms. (a) Excited state upconversion, (b) energy transfer upconversion, (c) cross-relaxation, (d) cooperative sensitization upconversion, (e) photon avalanche, (f) triplet–triplet annihilation.

process, one ion will go to a higher excited state E_2 through ESA. This ion will relax back to the lower excited state, E_1, and this energy will be transferred to the neighbouring ion through cross-relaxation energy transfer (CRET), which will be promoted to the E_1 excited state. Subsequently, both these ions will be promoted to the E_2 excited state and further, through CRET, they can excite two more ions, leading to a total of four ions in the E_1 state. In this manner, all the ions will populate the E_1 energy state. After this state, upconversion will proceed from the E_1 state without the involvement of the ground state. This PA process is highly efficient but is seldom observed in nanocrystals due to the requirement of a high pumping intensity.[27]

2.1.6. Triplet–triplet annihilation. The processes discussed above are commonly observed in inorganic frameworks, however, in molecular systems, upconversion occurs through triplet–triplet annihilation (TTA), which is a slight variation of ETU. The strong localization of excited states in the molecular systems gives rise to distinct singlet and triplet states. In this mechanism, a sensitizer absorbs a low-energy photon reaching the excited singlet state, and later on, it goes to the triplet state through inter-system crossing (ISC). A triplet-mediated energy transfer takes place from the sensitizer to the emitter, promoting it to the excited state. A similar process takes place with another sensitizer-emitter pair and finally, two emitters relax back to the ground state, emitting a higher energy photon.[28]

2.2. Materials

Upconversion nanocrystals include an inorganic host material and lanthanide dopant ions. Different combinations of hosts and dopants along with different dopant concentrations help to achieve the tunability of different photophysical properties, including emission wavelength and intensity. The following section of this review will focus on the different components of UC nanocrystals.

2.2.1. Host materials. A major criterion for tuning the properties of UC nanocrystals is choosing the appropriate host matrix. The intra-4f transitions are usually forbidden according to quantum mechanics rules. However, the crystal field of the host matrix interacts with the electron clouds of lanthanide ions, which enables the forbidden transitions and also affects the transition possibilities between different levels. Since the interactions are small, the 4f levels of lanthanides remain largely unchanged. However, these minute interactions relax the selection rules for radiative transitions and alter the probabilities of transitions between different energy levels.[29] Thus, choosing the right host material is crucial for efficient and highly intense luminescence.

Host matrices with low phonon energies are considered ideal for UC nanocrystals. Different halides, including chlorides, bromides, and iodides, have low phonon energies ($<300\ cm^{-1}$) but their hygroscopic nature restricts their applications. On the other hand, fluorides are highly stable and exhibit phonon energy

of around 500 cm^{-1}.[30] Hexagonal (β phase) $NaYF_4$ is one of the most efficient and most studied host matrices for green and blue emission due to its narrow crystal field splitting.[21,31] Along with these properties, this matrix is safer to grow due to the high solubility of NaF in water as compared to other rare earth fluorides, like $LiYF_4$, which require hazardous ammonium fluoride precursors.[32] Zhou *et al.* synthesized the nanowire morphology of β-$NaYF_4$ that could be optically trapped and refrigerated using a near-IR laser having potential applications in localized optoelectronic device cooling and laser refrigeration.[33] Some of the other synthesized fluoride matrices include $NaGdF_4$, $KGdF_4$, GdF_3, $NaEuF_4$,[34] CaF_2,[35] BaF_2,[36] $Na_3Li_3Sc_3F_{12}$,[37] *etc.* Host matrices having cations with radii similar to lanthanide dopants reduce the formation of crystal defects. Therefore, Na^+, Ca^{2+}, and Y^{3+} are superior host cations for UC materials.[38] Another class of commonly used host matrices is oxides, which have good thermal conductivity, isotropic optical properties, and chemical stability even at high temperatures and in corrosive environments. However, their phonon energy is generally higher than 500 cm^{-1}. Various ceramic-based oxides like Y_2O_3, La_2O_3, GdO_3, *etc.*, with low phonon energy, are known to be transparent to visible light and have low interaction with doped emitter ions similar to the fluoride hosts.[39] A number of oxide materials, including Al_2O_3,[40] TiO_2,[41] $Yb_3Al_5O_{12}$,[42] $Yb_2Ti_2O_7$,[43] $CaMoO_4$,[44] $PbMoO_4$,[45] $NaLa(MoO_4)_2$,[46] *etc.*, have been explored. Molybdenum oxides provide additional emission intensity due to their relatively low phonon energy.[47]

2.2.2. The effects of phonon energy on the host. Upconversion includes radiative emission when ions relax back to the ground state from excited states. Thus, any non-radiative loss, which usually requires phonons, would lower the emission efficiency but this phonon energy could be efficiently tailored to manipulate the emissive properties of the UC nanocrystal. For example, Fig. 3 shows two different ions with lattice phonon energies of 600 cm^{-1} and 1200 cm^{-1}. The case of the ion with a phonon energy of 600 cm^{-1} provides two possibilities of ion relaxation from the excited state to the ground state. Green luminescence will occur in the case of direct radiative emission from the excited state to the ground state, whereas red emission will occur through non-radiative emission to the lower-lying intermediate state. Since, in this case, the highest excited state and intermediate state are separated by a 5000 cm^{-1} gap, the probabilities of getting red emission are low. However, in the case of phonon energy of 1200 cm^{-1}, it would be easy to bridge the gap between the lower-lying intermediate state and the highest excited state, leading to more probable red emissions and less green emissions.[48]

2.2.3. Dopants. The dopant material in the nanocrystals plays a vital role in the absorption and emission of light, and lanthanides make the most promising materials for upconversion.[49–51] They have rich energy level patterns since their $4f^n$ configurations are split by electronic repulsions and spin–orbit coupling (shown in Fig. 5). The 4f–4f transitions are parity-forbidden, however, this selection rule is broken in the presence of two configurations with opposite parity. Also, the 4f–4f transitions are dipole-forbidden in lanthanides, which

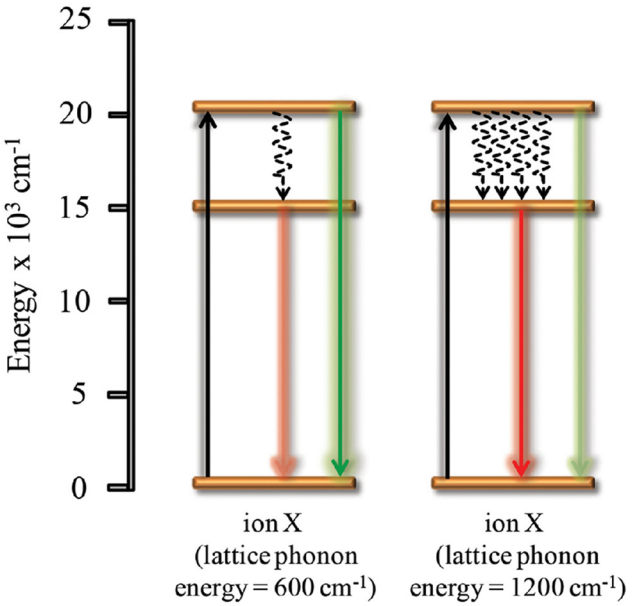

Fig. 3 The effect of lattice phonon energy on the luminescence properties of an ion. Reprinted with permission from Wiley.[48]

makes the decay times in the order of microseconds, giving rise to the opportunity for sequential excitations and energy transfers.[52] The electric dipole transition probability increases due to the presence of an asymmetric crystal field. The crystal field splitting of lanthanides (shown in Fig. 4) could also be modified using dopants of different sizes.[53] For example, Zheng *et al.* recently reported an increase in the emission intensity of $Yb^{3+}/Tm^{3+}/Ho^{3+}$ tri-doped $NaYF_4$ microcrystals when doped with 8 mmol% of Li^+. The emission intensity of blue (450 nm, 475 nm), green (541 nm), and red (648 nm) light increased by 2.75, 2.095, 2.65, and 2.87 times, respectively.[54]

Among the lanthanides, La^{3+}, Y^{3+} and Lu^{3+} do not have unpaired 4f electrons and are, therefore, suitable for host materials, and not as luminescent centres. Also, Gd^{3+} has fewer intermediate states and transitions results in the UV region, making it less suitable as a luminescent centre. However, Sm^{3+} ($4f^5$), Eu^{3+} ($4f^6$), Tb^{3+} ($4f^8$), Dy^{3+} ($4f^9$) and Ho^{3+} ($4f^{10}$) have adequate energy gaps for emissions in the visible region. In contrast, Nd^{3+} ($4f^3$), Er^{3+} ($4f^{11}$) and Tm^{3+} ($4f^{12}$) emit in the near-infrared region.[23]

Both the emitter and sensitizer need to be chosen carefully to obtain the required wavelength of emission. The role of a sensitizer is to absorb the incoming radiation and transfer it to the emitter ions. Therefore, ions having a larger cross-section area for absorption are ideal candidates for sensitizer ions. Further criteria that come into the picture is that the excited state of the sensitizer ions should be closer to the emitter ions making energy transfer efficient and easy. Thus, Yb^{3+}, having a cross-section area of 9.11×10^{-21} cm^{-2} at a wavelength of 980 nm and having only one excited state ($^2F_{5/2}$) matching with the f–f transitions of several emitter centres, makes an ideal sensitizer material. For example, the $^4I_{11/2}$ state of Er^{3+} overlaps

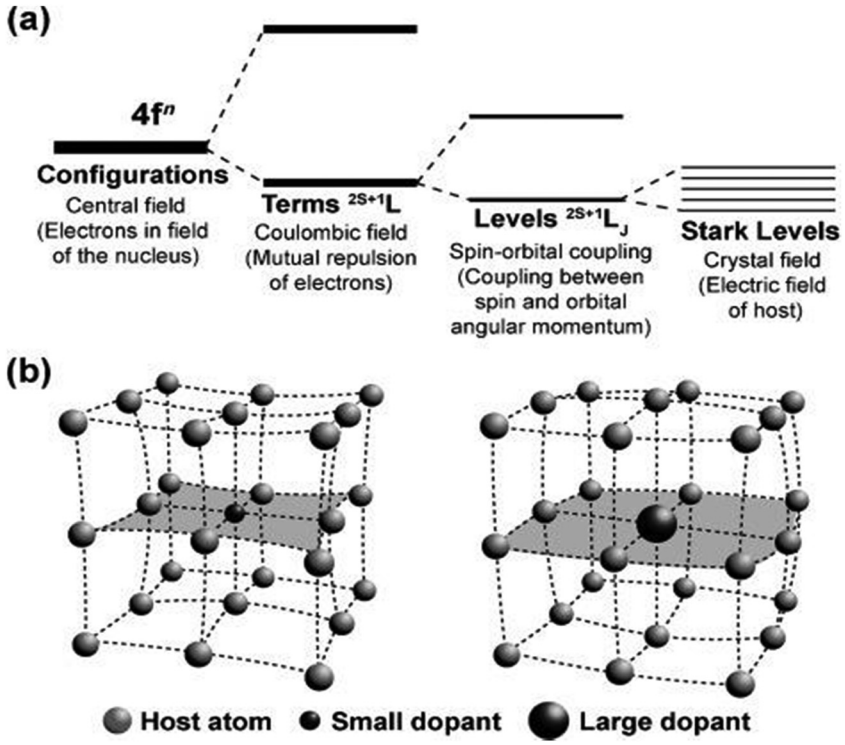

Fig. 4 (a) A simplified representation of the effect of the coulombic field, spin–orbit coupling, and crystal-field interaction on the [Xe]4f^n configuration. (b) Crystal lattice contraction (left) and expansion (right) as a result of the substitution of a host atom with dopants of varied sizes. Reprinted with permission from Wiley.[53]

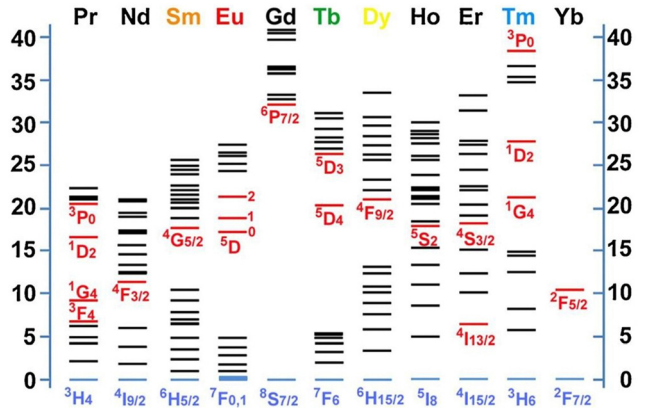

Fig. 5 Partial energy diagrams for the lanthanide aqua ions; the values of the energy levels are given as 1000 cm^{-1}. The red and blue lines indicate the main luminescence and the fundamental levels, respectively. Reprinted with permission from Elsevier.[57]

with the $^2F_{5/2}$ state of Yb^{3+} and allows energy transfer from Er to Yb.[55,56] The role of the emitter is to convert the photons with low energy into higher-energy photons. Therefore, sensitizer atoms having f–f transitions among different energy levels that could provide the required emission wavelength have to be chosen accordingly. For example, erbium dopants can convert incident radiation of 1.5 μm into the UV-Visible-NIR regions. Various combinations of lanthanides have been explored to achieve different wavelengths in the visible region as listed in Table 1.

3. Applications of upconversion materials in different kinds of solar cells

This upcoming section focuses on the application of upconversion nanomaterials in different kinds of solar cells and the enhancement in the power conversion efficiency along with integration strategies that have been adopted.

3.1. DSSC

Dye-sensitized solar cells (DSSCs) are potential candidates for replacing traditional silicon solar cells because of their low cost, high efficiency, and easy fabrication. They are considered green technology and they were first designed by O'Regan and Grätzel.[81] A typical DSSC is fabricated using a nanocrystalline TiO_2 semiconductor film on a transparent conductive oxide glass (TCO), a platinum-coated transparent conducting oxide glass as a counter electrode, and an electrolyte solution containing an I^-/I_3^- redox couple.[82] However, the light-harvesting capability of DSSC is a major limiting factor for the overall performance of the device.[83] The wavelength range for absorption (300–800 nm) largely remains the same even for different organic sensitizers like N3, N719, N749, *etc.* (shown in Fig. 6), due to higher charge recombination rates and poor charge injection efficiency.[84] Thus, a large part of the solar spectrum, including infrared and near-infrared light, is not utilized. The majority of the NIR component of the incident sunlight is lost as thermal heat and non-absorption photons, leading to a decrease in the ability of DSSCs to utilize this part of

Table 1 Excitation and emission wavelengths of various UCNPs

UCNP	Excitation (nm)	Emission (nm)	Ref.
YbF_3/Ho^{3+}	980	545, 750	58
$NaGdF_4$:Yb,Er	980	517–532, 532–551, 635–670	59
$Y_2O_3/Yb^{3+},Ho^{3+}$	980	545, 650, 779	60
$CeO_2/Er^{3+},Yb^{3+}$	980	520–560, 640–680	61
$BiYO_3/Er^{3+},Yb^{3+}$	980	520–570, 640–700	62
$NaYF_4$:Yb,Er@$NaGdF_4$:Nd@SiO_2	980	410, 520, 540, 655	63
$NaYF_4:Er^{3+},Yb^{3+}@SiO_2$	980	545, 655	64
$NaYF_4:Yb^{3+},Er^{3+}$@$NaYF_4:Nd^{3+}$ core	980	408, 525/540, 660	65
$LiYF_4:Er^{3+},Yb^{3+}$	980	546, 556, 674	66
TiO_2 nanorods: Er^{3+}	980	512–527, 536–560, 650–680	67
$LiGdF_4:Yb^{3+},Er^{3+}$	980	520, 540, 650	68
$NaYbF_4:Ho^{3+}$	980	540, 644, 750	69
$NaGdF_4:Er^{3+}/Yb^{3+}$	980	522, 540, 653	70
$SiO_2/NaYF_4:Yb^{3+},Er^{3+}@SiO_2$ core–shell	980	522, 540, 654	71
$NaYF_4:Yb^{3+},Tm^{3+}$	980	290, 345, 362, 451, 475	72
$NaCsWO_3$@$NaYF_4$@$NaYF_4:Yb^{3+},Er^{3+}$	980	540, 654	73
$NaYF_4:Yb^{3+},Er^{3+}$@$NaYF_4:Yb^{3+},Nd^{3+}$ core–shell	980	414, 526, 546, 660	74
Fluoroindate glass/Er^{3+},Yb^{3+}	1480	545, 650, 975	75
$NaYF_4:Er^{3+}$	980/1540	550/660	76
$SiO_2:YF_3:Er^{3+},Yb^{3+}$	1550	559, 653, 669, 803, 926, 970	77
$SiO_2/Al_2O_3:Er^{3+},Yb^{3+}$	1550	630–650	78
$CeO_2:Yb^{3+},Er^{3+}$	980/1540	550/665	79
$NaYF_4$:Yb/Er/Gd	980	524, 540, 660	80

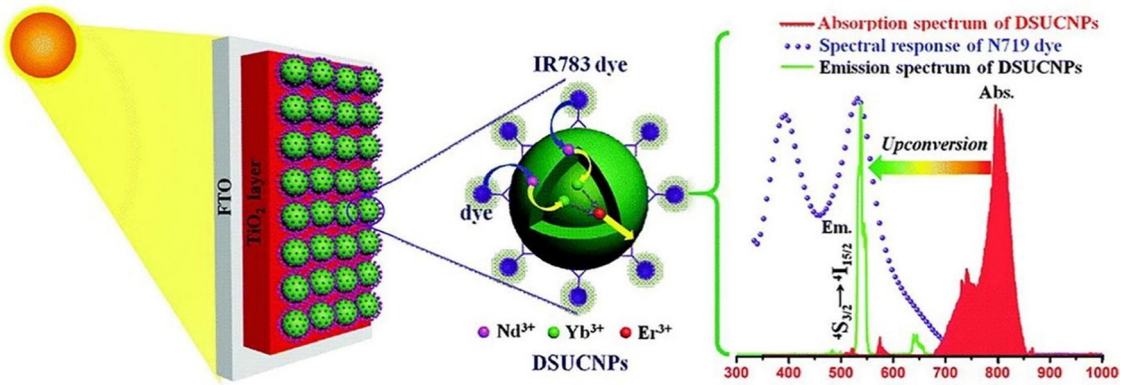

Fig. 6 Broadband near-infrared sunlight harvesting and spectral conversion into the visible range to activate the N719 dye for the improvement of a DSSC device. Reprinted with permission from Elsevier.[84]

the spectrum. Therefore, upconversion finds its application in DSSCs to broaden the absorption spectrum and utilize the sub-band gap photons. Also, for a solar cell with a 1.7 eV band gap (similar to DSSC), it has been shown that the SQ efficiency limit can be improved using upconverters from 28.2% to 43.6%.[85]

UCNPs were combined with DSSCs for the first time by Shan and Demopoulos. They reported a TiO_2-UCNP (Yb^{3+}, Er^{3+} co-doped LaF_3) nanocomposite working electrode to improve NIR light-harvesting in dye-sensitized solar cells.[86] Thereafter, a large number of UCNPs have been explored in the field of DSSCs. Yu *et al.* synthesized nano-heterostructures of YbF_3–Ho/TiO_2 for use as new photoelectrode materials. They combined the upconversion properties with the semi-conductive properties of TiO_2, which enhanced the overall absorption by utilizing the near-infrared light, as well as improved the photoinduced charge separation by increasing the lifetime of excited electrons. An enhancement of 19% was achieved in the photocurrent and the overall power conversion was enhanced by 23%, reaching 8%.[58]

Another group of researchers, Ramaswamy *et al.*, investigated the synergistic effects of UCNP β-$NaGdF_4$:Yb,Er,Fe with light-reflecting silver nanoparticles (150 nm). They observed a bright green emission under a 980 nm laser, also visible to the naked eye. The first green emission is in the range of 517 to 532 nm, corresponding to $^2H_{11/2} \rightarrow {}^4I_{15/2}$ transition and the other is in the range from 532 to 551 nm, corresponding to $^4S_{3/2} \rightarrow {}^4I_{15/2}$ transition. A red emission from 635 to 670 nm was also observed, attributed to the $^4F_{9/2} \rightarrow {}^4I_{15/2}$ transition. The resonance frequency of silver nanoparticles overlaps with the green and red emissions of the UCNPs. Through the effective coupling of these effects, they achieved an efficiency enhancement of 21.3% with the application of a silver rear reflector combined with upconversion nanoparticles, and the overall efficiency increased from 5.08% to 7.04%.[59] To solve the toxicity

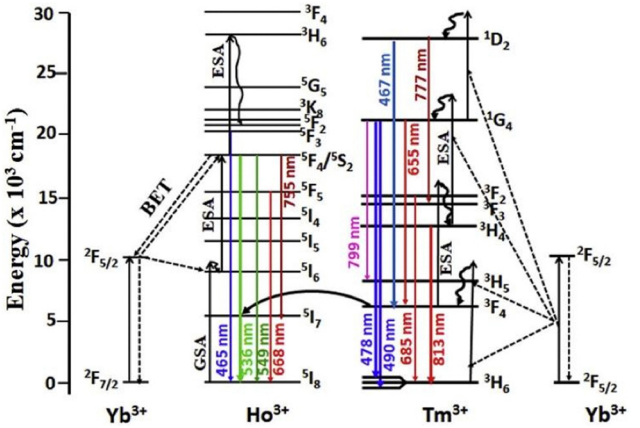

Fig. 7 Energy level diagrams of Ho^{3+}–Yb^{3+}–Tm^{3+} ions and the possible UC and ET processes under 976 nm excitation. Reprinted with permission from Elsevier.[60]

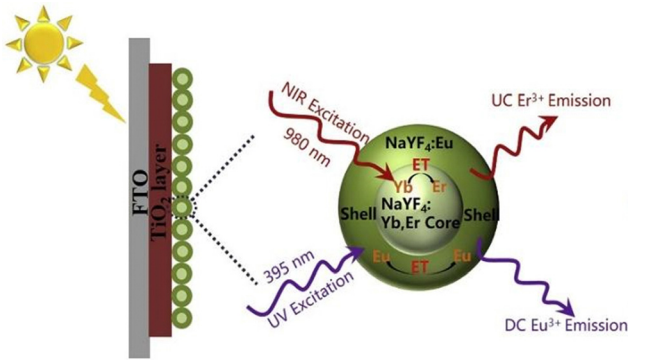

Fig. 8 Near-infrared and ultraviolet sunlight harvesting, and spectral conversion into the visible range to activate the N719 dye for the enhancement of a DSSC device. Reprinted with permission from Elsevier.[87]

and chemical stability issues of fluorides, many oxide UCNPs have been explored. Tadge *et al.* explored the colour tunability of the tri-doped Y_2O_3 matrix. The Ho^{3+}/Yb^{3+} doped matrix gives weak red and intense green emission, whereas Tm^{3+}/Yb^{3+} emits NIR and blue emission with a 976 nm excitation wavelength. However, the tri-doped Y_2O_3:$Tm^{3+}/Ho^{3+}/Yb^{3+}$ UCNP emits intense green light at 976 nm. They also investigated changes in emission with different doping concentrations of Yb^{3+}, proving the colour tunability (shown in Fig. 7) of the system, which is present in both co-doped and tri-doped UCNPs. The tri-doped nanophosphor also exhibited the Yb^{3+} concentration-dependent depopulation of Ho^{3+} ions in $^5S_2$ and $^5F_4$ levels due to the presence of back energy transfer (BET) phenomena, which take place as follows:

$$Ho^{3+}(^5S_2,{}^5F_4) + Yb^{3+}(^2F_{7/2}) \rightarrow Ho^{3+}(^5I_6) + Yb^{3+}(^2F_{5/2}).$$

The tri-doped matrix yielded an increase in open-circuit voltage by 8.46% and short-circuit current density by 5.18%. This resulted in a 10.33% increase in PCE as compared to bare TiO_2-based solar cells.[60] More recently, Ambapuram *et al.* synthesized CeO_2:Er^{3+}/Yb^{3+} UCNPs for upconversion and scattering layer on bilayer counter electrodes of SnS and PEDOT:PSS. The as-fabricated DSSC achieved a fill factor of 0.71 with a V_{OC} of 0.64 V, and J_{SC} of 18.48 mA cm^{-2} with an overall power conversion efficiency of 8.41%.[61] Dutta *et al.* worked on $BiYO_3$:Er^{3+}/Yb^{3+} UCNPs that exhibited emission bands resulting from $2H_{11/2} \rightarrow {}^4I_{15/2}$, $^4S_{3/2} \rightarrow {}^4I_{15/2}$ and $^4F_{9/2} \rightarrow {}^4I_{15/2}$ transitions. They achieved a power conversion efficiency of 6.20% from the previous 5.73%.[62]

The light trapping capability of the UCNPs can be enhanced by developing the core–shell nanostructure, where the shell layer transfers energy to the core more efficiently. Adopting this strategy, Zhang *et al.* synthesized the core–shell nanostructure of $NaYF_4$:Yb,Er@$NaGdF_4$:Nd@SiO_2 and studied the synergistic effects with TiO_2 hollow spheres (HS). Here, the TiO_2 HS layer is used as a scattering center. Both the UC core–shell nanostructure and HS were applied on the TiO_2/FTO photoanode coated with N719 dye to design a DSSC. The incorporation of the core–shell UCNP in this heterostructure enhanced the PCE by 26.93%.[63] The enhancement of the photovoltaic efficiency is due to upconversion as well as the size-dependent light scattering of the nanoparticles. However, Zhou *et al.* demonstrated the contribution of UCNP in enhancing the efficiency of DSSC using the $NaYF_4$:Er^{3+},Yb^{3+}@SiO_2 core–shell geometry where the size-dependent factor was eliminated. The emission peaks were observed at 543 nm and 655 nm for $^4S_{3/2}$ to $^4I_{15/2}$ and $^4F_{9/2}$ to $^4I_{15/2}$ transitions, respectively. The short-circuit current was enhanced by 4% (from 12.35 mA to 13.03 mA) along with a PEC enhancement of 6.37% due to the presence of UCNP.[64] Hao *et al.* reported an alternate strategy to further improve the PCE by designing a core–shell architecture of UCNP with IR783 organic dye. The dye showed a broad and efficient NIR-harvesting capability due to a larger molecular absorption cross-section (10–17 cm^2) as compared to the narrow and inefficient absorption of UCNP in the NIR region. Here, Nd^{3+} is acting as a sensitizer and transmitting the absorbed NIR light to the Yb/Er core, resulting in 540/650 nm emission with an enhancement in upconversion luminescence by 9-fold and PCE by 13.1%.[65] Interestingly, the broadband absorption was further extended with the development of the upconversion and downconversion strategies *via* the alternation of doping elements in core/shell matrices. Chen *et al.* demonstrated that the doping of Yb^{3+}/Er^{3+} in the core matrix for upconversion and Eu^{3+} in the shell matrix for downconversion (shown in Fig. 8) cumulatively harvested the NIR and UV regions, respectively, increasing the overall PCE by 13.95%.[87] The choice of doping elements plays an important role in overall efficiency, and the selection of the host matrix contributes significantly to modulating the photoconversion efficiency.

Commonly, a fluoride matrix provides low phonon energy and induces luminescence quenching due to impurities and surface defects (shown in Fig. 10). Tian *et al.* showed that the decoration of a native oxyfluoride layer (YOF:Yb^{3+}/Er^{3+}) on the $NaYF_4$:Yb^{3+}/Er^{3+} core geometry *via* high-temperature annealing suppresses the surface quenching and modulation of the phonon energy of the core host matrix. Thereby, the red-to-green emission ratio was modulated from 1.3 to 11.2 at an

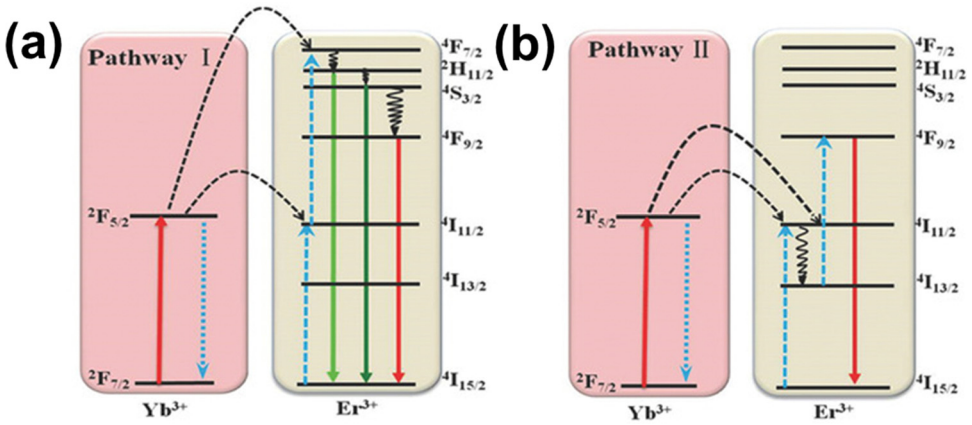

Fig. 9 The energy levels of the Yb^{3+}/Er^{3+}-codoped $NaYF_4$:Yb^{3+}/Er^{3+}@YOF:Yb^{3+}/Er^{3+}, showing possible energy transfer upon 980 nm excitation. Reprinted with permission from Wiley.[88]

optimized annealing temperature of 600 °C. It was observed that a gradient interface was formed due to a huge lattice mismatch between the cubic phase of YOF and the hexagonal phase of $NaYF_4$, helping to shield the emitter ions against quenching, and resulting in the effective coupling of photoelectrons and phonons of YOF:Yb^{3+}/Er^{3+}. Two pathways (shown in Fig. 9a and b) for upconversion have been identified for the photon population in the $^4F_{9/2}$ excited state when Yb^{3+} ions are excited directly. The first pathway includes the excitation of Er^{3+} ions to the $^4F_{7/2}$ state by Yb^{3+} ions through 980 nm light. This can lead to non-radiative transitions to $^2H_{11/2}/^4S_{3/2}$ and $^4F_{9/2}$. The transition from these levels to the ground state $^4I_{15/2}$ leads to green and red emissions, respectively. The second pathway occurs when Er^{3+} ions are excited to $^4I_{11/2}$, followed by non-radiative relaxation to $^4I_{13/2}$. Further transition to $^4F_{9/2}$ followed by relaxing back to $^4I_{15/2}$ results in red emission. Here, the non-radiative transitions in both pathways compete and thus, in the case of a fixed energy gap, the probability of the transition is related to the phonon energy of the host matrix. With the increase in phonon energy, the transitions from $^4I_{11/2} \rightarrow {}^4I_{13/2}$ and $^4S_{3/2} \rightarrow {}^4F_{9/2}$ will increase, giving rise to a high R/G ratio. Therefore, the formation of the YOF shell on the $NaYF_4$:Yb^{3+}/Er^{3+} host matrix increases the phonon energy, leading to a significant improvement in the R/G ratio. This as-synthesized UCNP modulates better NIR absorption and thereby enhances the PCE by 17% (Fig. 10).[88]

The upconversion nanoparticles showed remarkable improvement in the efficiency of DSSCs. This could be further improved by utilizing UCNPs with greater luminescence intensity developed by designing different morphologies under variable host matrices. Further, the use of dyes as shell materials of UCNPs provides greater light-harvesting opportunities because the high absorption coefficients of the organic dye molecules cumulatively impact and improve the photovoltaic performance.

3.2. Perovskite solar cells

Perovskite-based solar cells (PSC) are seen as future substitutes for conventional solar-powered conversion technologies including the traditional silicon solar cell. Within a short period, the efficiency of the perovskite solar cells has increased from the first reported 3.8% to as high as 26%, recently.[89] This improvement in efficiency makes it a potential candidate for the future

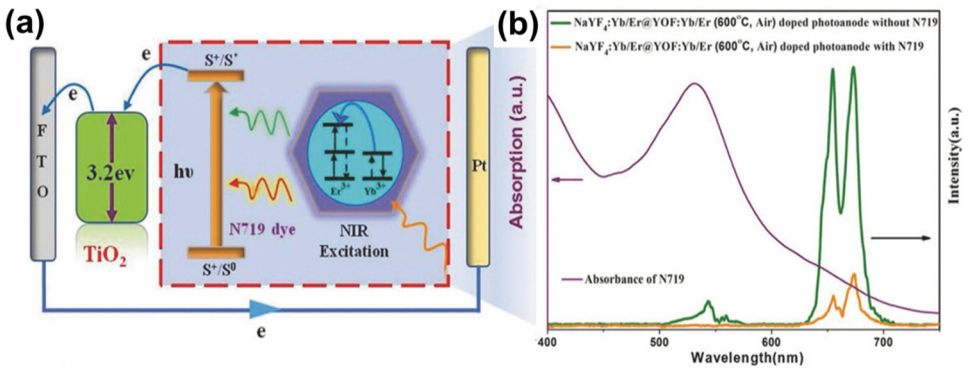

Fig. 10 (a) Energy diagram illustrating the NIR light-harvesting by the N719 dye through the UC process, the charge injection into TiO_2 and the transport of photoelectrons to the electrode surface. (b) The absorption spectra of the N719 dye and the UC emission spectra of TiO_2 photoanodes with $NaYF_4$:Yb^{3+}/Er^{3+}@YOF:Yb^{3+}/Er^{3+} (600 °C, air) before and after immersion in N719 dye. Reprinted with permission from Wiley.[88]

of the photovoltaic industry. However, perovskite solar cells are still struggling with issues like stability, toxicity (from lead-based perovskites), large-scale production, *etc.*[90] One important criterion that could help to further increase the efficiency would be to harvest photons more efficiently. The most common $MAPbI_3$-based perovskite could only harvest 50% of the total available sunlight at a wavelength of less than 800 nm. Thus, the upconversion mechanism finds its application prospects in enhancing the light-harvesting capacity of perovskite solar cells. Further, the UCNPs could be used in all three different layers of the device including the active layer, a hole-transporting layer, and an electron-transporting layer.[91] This section will discuss the different integration strategies adopted in perovskite solar cells.

Chen *et al.* made a primary investigation of the effects of upconversion on the efficiency of solar cells using $LiYF_4$ co-doped with Yb^{3+} and Er^{3+} single-crystals integrated on top of a perovskite solar cell (shown in Fig. 11). The single-crystal morphology also helps in removing the luminescence quenching effects due to defect states and serves as a transparent layer. This UCNP yielded a dominant green emission, which is dependent on the excitation power density. This resulted in an overall efficiency enhancement of 7.4% under sunlight simulated with a solar constant of 7–8.[66] However, introducing the UCNPs into the solar cell architecture provides the additional benefits of reduced light reflections. In this aspect, Zhang *et al.* investigated the performance of organo-mixed halide ($CH_3NH_3PbI_{3-x}Cl_x$) perovskite solar cells with Er^{3+}-doped nanorod arrays synthesized through a hydrothermal route. The TiO_2 nanorod architecture provides faster electron transport and Er doping modifies the band gap of TiO_2 from 3.00 eV to 3.07 eV and converts IR to green light emission. The Er-doped TiO_2 nanorods showed better absorption intensity in the UV region than undoped nanorods. A blue shift was also observed in the optical absorption edge, which could be attributed to the charge transfer transition between the 4f orbital electrons of Er^{3+} ions and TiO_2 valence or conduction bands. This resulted in an increase in PCE from 10.6% to 16.5% as compared to the un-doped TiO_2 nanorod configuration.[67] These UCNP could also be combined with the hole-transporting layer as demonstrated by Deng *et al.* They integrated the $Li(Gd,Y)F_4$:Yb,Er upconversion material into the spiro-OMeTAD-based hole-transporting layer. The Li-based matrix provided a higher luminescence intensity as compared to the $NaYF_4$ counterpart with the additional benefit of thermal stability under the same doping conditions. This matrix has a tetragonal bipyramidal morphology (shown in Fig. 12) with an intense green emission, which could be considered pure due to an acute emission peak and a high green-to-red ratio. The optimal concentration of UCNP was found to be 0.10 wt% after which the device performance degraded. This resulted in an overall PCE of 18.34% and an enhancement of over 25% with the upconversion nanoparticles.[68]

Another major issue that hampers the efficiency of perovskite solar cells is the charge recombination. The doping of upconversion nanoparticles into various layers of the solar cell also helps to reduce the effects of charge recombination and, thus, enhances the photoconversion efficiency. Li *et al.* fabricated a hole-conductor-free perovskite solar cell employing the synergistic effects of $NaYbF_4$:Ho^{3+} and ZrO_2 as a scaffold layer

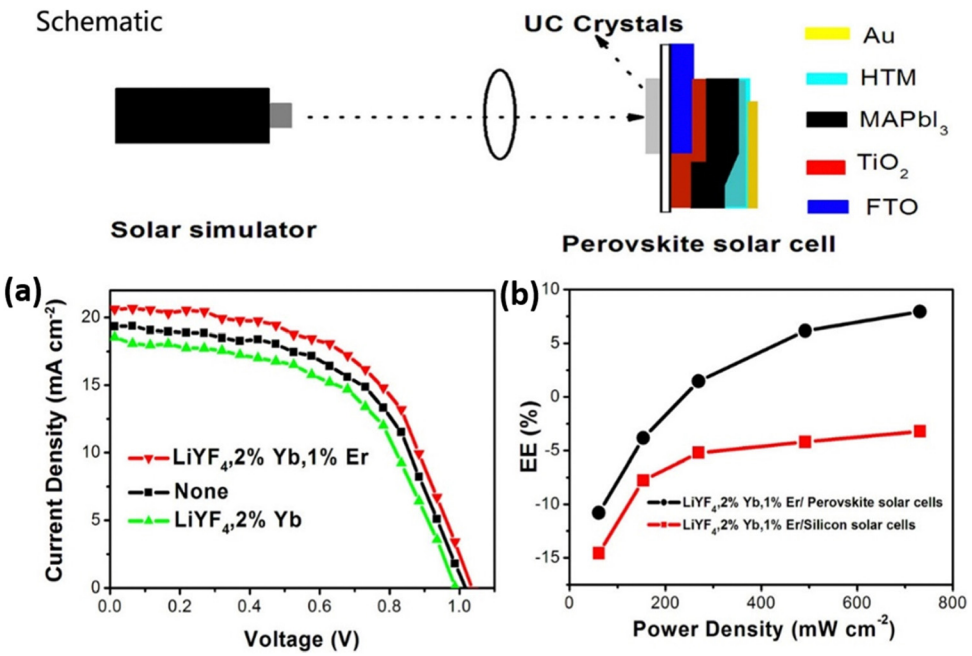

Fig. 11 A schematic representation of the perovskite solar cells under the simulated sunlight excitation. (a) *J*–*V* curves of the perovskite solar cells: $LiYF_4$:2%Yb^{3+},1%Er^{3+} crystals, $LiYF_4$:2%Yb^{3+} crystals, and no crystals, obtained under simulated solar illumination with an intensity of 0.73 W cm^{-2}. (b) Enhancement efficiencies (EE) of the perovskite solar cells and silicon solar cells with $LiYF_4$:2%Yb^{3+},1%Er^{3+} crystals dependent on the excitation power density. Reprinted with permission from the American Chemical Society.[66]

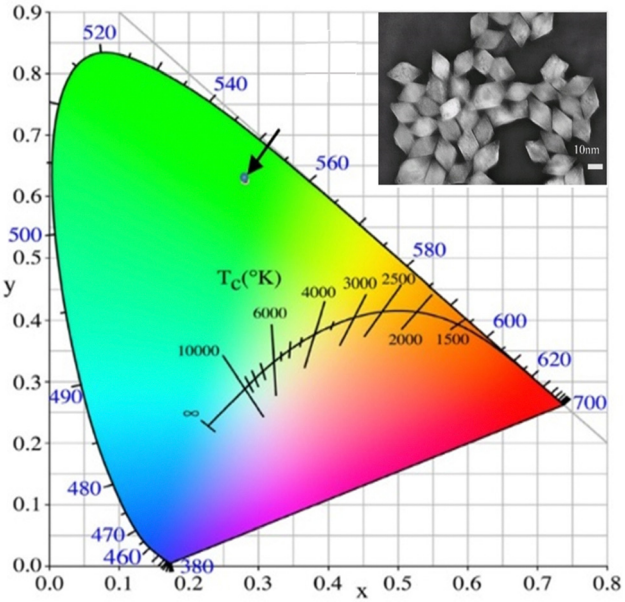

Fig. 12 The CIE chromaticity diagram of Li(Gd,Y)F_4:Yb,Er (inset: the TEM image of Y^{3+}-doped LiGdF_4:Yb^{3+},Er^{3+} upconversion nanocrystals). Reprinted with permission from Elsevier.[68]

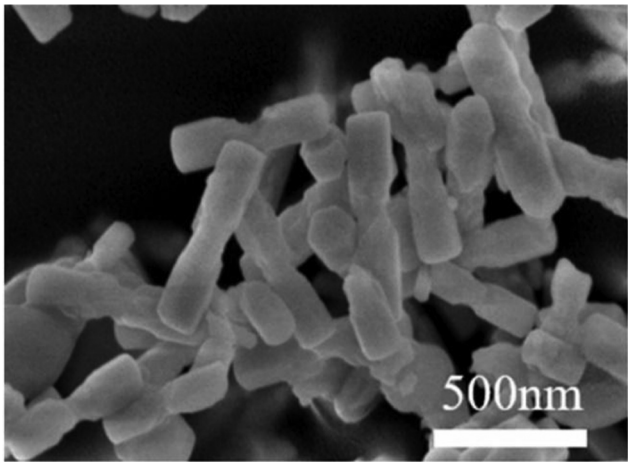

Fig. 13 SEM image of NaGdF_4:Yb^{3+},Er^{3+} nanoparticles. Reprinted with permission from Elsevier.[70]

in $FA_{0.4}MA_{0.6}PbI_3$ perovskite solar cells. They observed a flake-like morphology, which depends on the reaction time, and obtained heterogeneous grain sizes at reaction times of 5, 10, 15 and 15 h. A uniform, spherical grain size was obtained for the reaction times of 20 and 24 h. An FTO/compact TiO_2(cp-TiO_2)/(mesoporous)mp-TiO_2/mp-ZrO_2/$FA_{0.4}MA_{0.6}PbI_3$/CE-based perovskite solar cell was fabricated. Three emission peaks were observed at 540 nm, 640 nm and 750 nm, corresponding to $^5S_2$, $^5F_4 \rightarrow {}^5I_8$, $^5F_5 \rightarrow {}^5I_8$ and $^5S_2$, $^5F_4 \rightarrow {}^5I_7$ transitions, respectively. Here, 540 nm is the dominant peak giving fluorescent green emission. It was observed that the UCNP and ZrO_2 combination led to fewer holes in the scaffold layer, creating a smooth interface. This design also provided an additional benefit of a reduced electron–hole recombination rate along with NIR harvesting. The major areas where recombination could occur are the grain boundaries but, in this case, the large grain sizes reduced the surface and bulk defects. The UCNP further filled the pinholes present in ZrO_2, reducing the leakage current and the band gap was modified from 3.46 eV for ZrO_2 to 3.37 eV for the UCNP-doped ZrO_2 layer. With an optimum concentration of 40 wt% of UNCP, a PCE of 14.32% was achieved. A further increase in concentration led to a decrease in the short-circuit current density. Overall, lower recombination rates, lower trap density and enhanced light harvesting in the NIR region led to the better efficiency of the as-designed solar cell.[69]

More recently, Wu *et al.* explored another nanorod architecture where the synthesized NaGdF_4:Yb^{3+},Er^{3+} nanorods (shown in Fig. 13) were the upconversion material. However, the enhancement in photocurrent due to the infrared region is very low. The enhancement in efficiency was achieved due to lower defect states obtained through the modification of the perovskite by the UCNP and lower charge carrier recombination. Thus, an overall power conversion efficiency of 21.1% was achieved.[70] Adopting a similar approach, Qi *et al.* developed a hole transport-free perovskite solar cell. The SiO_2/$NaYF_4$:Yb,Er@SiO_2 core–shell structure doped in TiO_2 nanorods (shown in Fig. 14) was explored. The absence of hole-transporting material (HTM) reduced the cost of production and provided better stability. The core–shell architecture reduced the detrimental charge recombination that is present in the exposed $NaYF_4$ crystals due to the presence of defects and surface ligands. The pinholes present in the $NaYF_4$:Yb,Er@SiO_2 film led to better infiltration of perovskite between SiO_2 particles. The presence of an insulating layer above TiO_2 nanorods prevented direct contact with the carbon counter electrode and enhanced the charge transport by reducing charge carrier recombination. A power conversion efficiency of 14.52% was obtained using this hole transport-free architecture along with the contribution of UNCP.[71]

Apart from surface charge recombination, pinholes also have a deteriorating effect on the efficiency of solar cells. As a remedy, Qiu *et al.* studied the modification of $MAPbI_3$ films with β-$NaYF_4$:Yb,Er upconversion nanocrystals. The upconversion matrix was sandwiched between the perovskite and hole-transporting layer (HTL). It was found that the UNCPs also acted as pin-hole filling material and reduced the surface charge recombination along with upconversion. The UNCP materials are hydrophobic, thus contributing to the stability of the solar cell. The smoothness of the interface between the HTL and perovskite increased light absorption for wavelengths higher than 500 nm. This configuration reached an efficiency of 15.7% and was stable in an air atmosphere after 720 hours of storage.[92]

To further enhance the power conversion efficiency, the effects of surface plasmon resonance could be combined with the upconversion process. Park *et al.* investigated the effects of the silica-coated $NaYF_4$:Yb^{3+},Er^{3+} upconversion material between the hole-transporting material and the gold electrode. They explored the combined effects of upconversion and

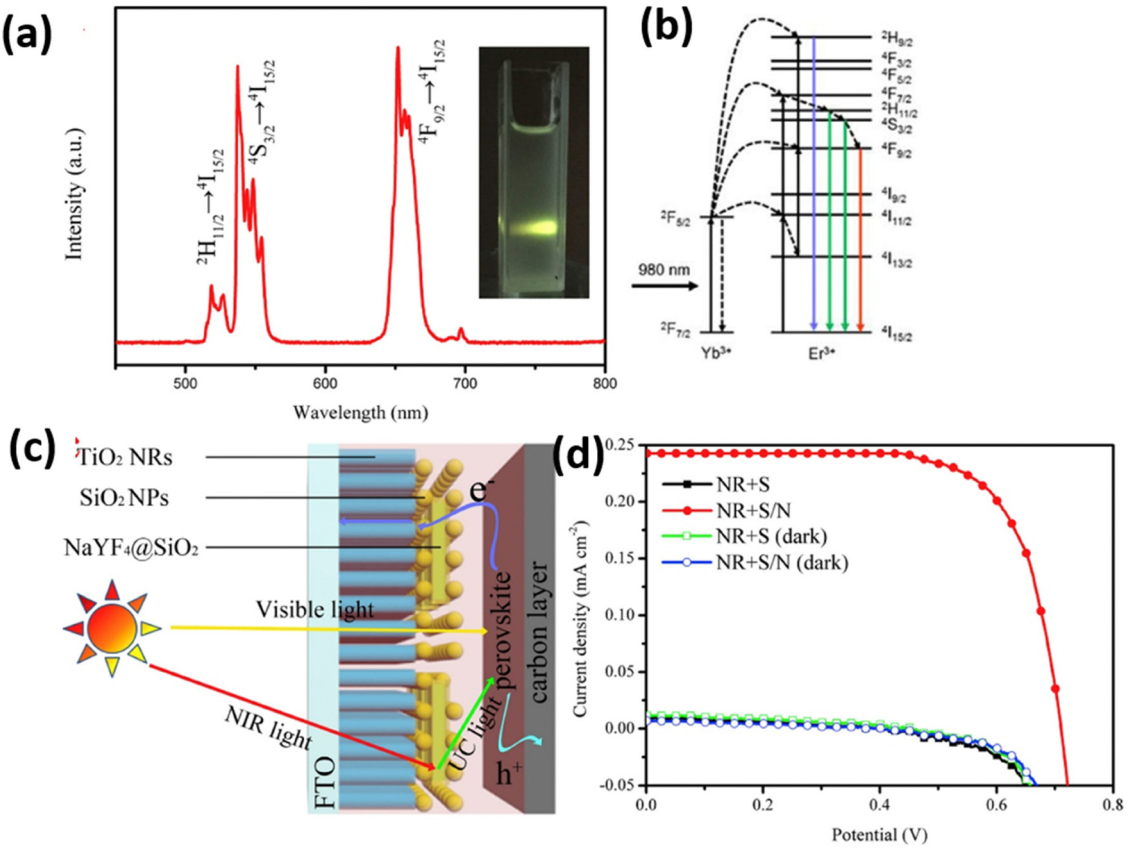

Fig. 14 (a) PL spectra of the $NaYF_4$:Yb,Er@SiO_2 under a 300 mW 980 nm NIR laser excitation; the inset is a photograph of the $NaYF_4$:Yb,Er@SiO_2 under a 300 mW 980 nm NIR laser excitation. (b) Energy-level diagram and the corresponding energy transitions in the $NaYF_4$:Yb,Er system. (c) Schematic diagrams of the energy transfer process in PSCs. (d) *J*–*V* curves of PSCs based on TiO_2 NRs with a SiO_2 or SiO_2/$NaYF_4$:Yb,Er@SiO_2 insulating layer obtained under irradiation by a 300 mW 980 nm NIR laser. Reprinted with permission from Elsevier.[71]

surface plasmon resonance. A dry transfer method utilising polydimethylsiloxane (PDMS) was used for transferring the UCNP due to its hydrophobic nature. The contribution from upconversion was found to be rather low (~1%); however, surface plasmon resonance is beneficial for solar cell efficiency. The UNCP deposited on gold film induced strong electromagnetic fields at the sharp Au bottom cores, which could interact with the UCNP layer. The reflection from the Au layer also contributed to the recycling of NIR light. They also studied the effects of UCNP on the solar cell performance when used with the perovskite layer and as an electron transporting layer (ETL) and obtained power conversion efficiencies of 14.40% and 11.07%, respectively, as compared to the 13.61% for the solar cell without upconversion material. The UCNP layer between the ETL and perovskite was found to be detrimental to the performance of the solar cell as the insulating nanoparticles added to the sheet resistance of the cell. However, the highest efficiency of 15.56% was achieved when the UNCPs were coated below the gold electrode.[89] Ma *et al.* investigated another fabrication strategy for perovskite solar cells where a double layer of upconversion material was used next to the rear (Au) and front (FTO) electrode having device fabrication in the following manner: FTO/c-TiO_2/UCNPs/perovskite/UCNPs/spiro-OMeTAD/Au. A β-$NaYF_4$ doped with Yb^{3+} and Tm^{3+} was used as the upconversion material. The scattering effect of UCNP reflected the light into the perovskite layer promoting a better photoresponse. This encapsulated matrix provided long-term stability under the open environment of 20–25% relative humidity at 25 °C, retaining up to 80% of the initial power conversion efficiency after 846 hours. The PCE was improved from 15.2% to 18.2% using the upconversion material. The bottom and top layers of UCNP also contributed to better electron transport and smooth film morphology that increased the fill factor (FF) and open circuit voltage (V_{OC}), whereas, the upconversion effect increased the short-circuit current density.[72] Xu *et al.* also studied the effects of surface plasmon resonance for boosting the upconversion luminescence for the $NaCsWO_3$@$NaYF_4$@$NaYF_4$:Yb,Er matrix. The upconversion luminescence intensity was enhanced more than 124 times using the optimum amount of $NaCsWO_3$ (2.8 mmol%) and adding in the spiro-OMeTAD layer. The overall efficiency increased from 17.99% to 18.89% for the device with UCNPs (shown in Fig. 15).[93]

Another strategy is to use the upconversion material along with organic dyes. Bi *et al.* investigated the effect of $NaYF_4$:Yb_{3+},Er_{3+}@$NaYF_4$:Yb^{3+},Nd^{3+} core–shell nanoparticles, along with dye sensitisation by IR-783 dye coupled with plasmonic Au nanorod (AuNR) film (shown in Fig. 16). For nanoparticles of

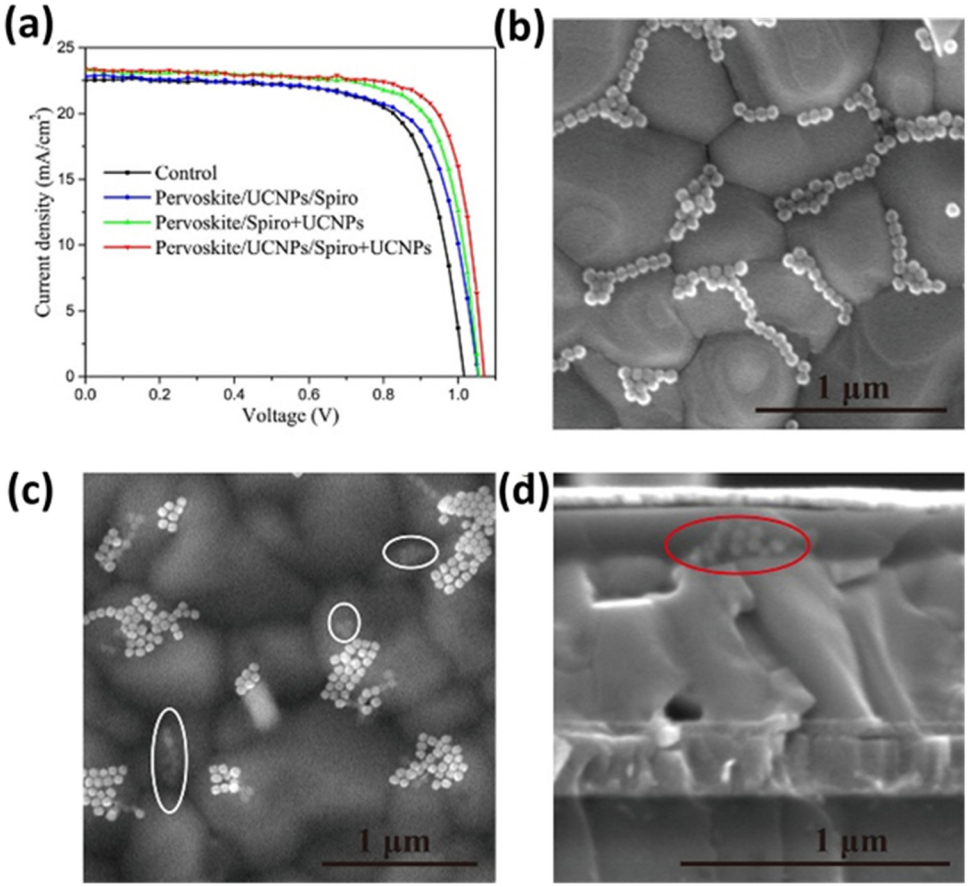

Fig. 15 (a) *J*–*V* characteristics of several types of PSCs. Top-view SEM images of (b) perovskite/UCNP film and (c) perovskite/UCNP/spiro + UCNP film. (d) Cross-sectional SEM images of the PSC with the structure of ITO/SnO_2/perovskite/UCNPs/spiro + UCNPs/Au. Reprinted with permission from the American Chemical Society.[93]

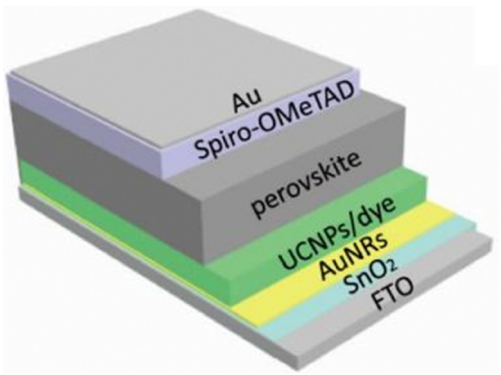

Fig. 16 The structure of PSCs and the scattering and reflecting mechanism diagram. Reprinted with permission from the American Chemical Society.[74]

less than 20 nm, the luminescence quantum efficiency is in the range of 0.1–1%, thus an enhancement in the absorption cross-section is essential. The dye layer acts as an antenna to absorb a broad band of light. Oleic acid at the surface of the UCNPs was removed through a ligand exchange reaction that connected dye molecules to the surface. There must be an efficient energy transfer between the dye molecules and Nd^{3+} ions, which was confirmed by the fluorescence decay curves of the IR-783 dye with and without UCNP. A decay in the lifetime of the IR-783 dye from 1.3 ns to 0.69 ns could be due to Fluorescence Resonance Energy Transfer (FRET) from dye molecules to Nd^{3+} ions. The energy transfer efficiency was calculated as follows:

$$\mathrm{ET} = 1 - \frac{\tau_{\mathrm{DA}}}{\tau_{\mathrm{D}}}$$

where τ_{D} represents the decay time in the absence of an acceptor and τ_{DA} represents the decay time in the presence of acceptor ions. Around 47% energy transfer efficiency from IR-783 to Nd^{3+} was observed. An upconversion luminescence enhancement of around 35 times was achieved with the help of dye sensitization and this number reached 120 times when coupled with AuNRs. This efficiency enhancement is dependent on the concentration of the dye and also on the size of the UCNPs. The optimal dye concentration that gave maximum results was 7.5 μg ml^{-1}, after which the efficiency decreased with increasing concentration. This is because on increasing the dye concentration, more light was absorbed but could not be transferred to UCNPs and the interactions between dye

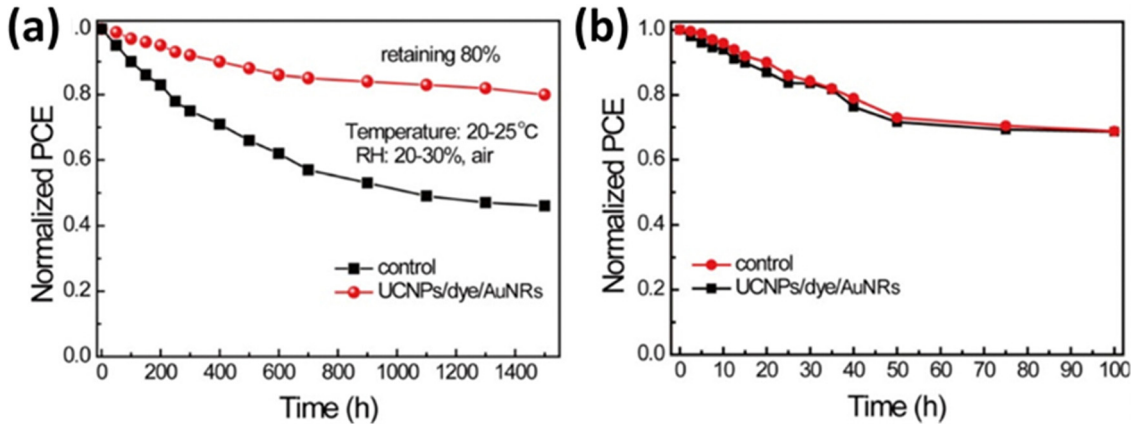

Fig. 17 (a) The stability of devices for a control film and a film incorporating a UCNPs/IR-783 dye/AuNRs composite film under an air environment, RH = 20–30% and 20–25 °C. (b) Light stability of devices for a control film and a film incorporating a UCNPs/IR-783 dye/AuNRs composite under AM 1.5G irradiation. Reprinted with permission from the American Chemical Society.[74]

molecules led to surface quenching. Ultimately, this nanocomposite film increased the power conversion efficiency from 19.4% to 21.1% when incorporated into the SnO_2 layer of the perovskite solar cell and also enhanced the stability (shown in Fig. 17) of the solar cell.[74]

The perovskite solar cells have ample integration strategies for the incorporation of upconversion nanoparticles at different stages of the device fabrication, which are projected towards better photovoltaic performance. However, different levels of efficiencies have been achieved by the incorporation of UCNPs into different layers of the device. Thus, to achieve the maximum PCE, a variety of combinations of UCNPs with perovskite and other layers of the solar cell needs to be adopted along with the strategies to enhance the luminescence intensity of the upconversion nanoparticle itself.

3.3. Silicon solar cells

The enhancement of the efficiency of silicon solar cells, as they continue to dominate the solar cell market, remains an intriguing topic for researchers. They can utilize the solar spectrum up to 1100 nm but the mid-IR range largely goes unutilized, comprising a 20% share of the overall solar spectrum. This unutilized part of the spectrum provides the opportunity to improve the photoconversion efficiency of the existing silicon solar cell technology.[94] While there have been several studies on DSSC and perovskite solar cells, the integration of upconversion nanoparticles in silicon solar cells remains unexplored. Various sophisticated deposition techniques play major roles in thin film solar cells, whereas the synthesis of UCNPs is mainly through the chemical synthesis route. The requirement of low phonon energy also hampers the possibility of doping lanthanides into various kinds of thin films. To overcome this challenge, a simple strategy of doping the upconversion material into a glass has been adopted, where this glass would be kept at the top of the photovoltaic device.

Working on a similar pathway, Rodriguez *et al.* studied the effects of Yb^{3+} and Er^{3+}-doped fluoroindate glass on the performance of a commercially available silicon solar cell.

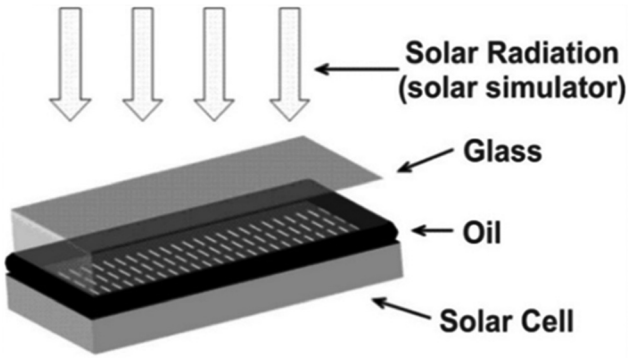

Fig. 18 A Si solar cell covered with glass and the matching oil. Reprinted with permission from Elsevier.[95]

The Yb^{3+} and Er^{3+} ions have the capability of absorbing solar radiation at 1.54 μm. Yb^{3+} acts as a sensitizer due to its large cross-section area. Also, the chosen host matrix is fluoroindate glass, which provides very low phonon energy that necessitates at least 20 phonons for a non-radiative transition and, therefore, serves as a suitable host material for an upconverter. It has been found that the UC emission depends on the concentration of Er^{3+} ions with 0.1 mol% of Yb^{3+}, where the most efficient performance was observed with 2.25 mol% of Er^{3+}. The upconverter matrix was simply placed on the Si solar cell without using an index-matching oil, and the external quantum efficiency (EQE) was significantly improved with 37 mW excitation.[96] More recently, Gracia *et al.* used a tellurite glass codoped with Eu^{3+} and silver nanoparticles for downconversion-induced enhancement in solar cells. The fabrication strategy was to use the UCNP on a glass substrate with a refractive index of 1.5, which was kept above the solar cell using oil (shown in Fig. 18) with a refractive index of 1.9 as an interface. Both the refractive indices should be close to each other to reduce the reflection coefficient. The oil interface ensures good optical contact between both elements and also reduces reflection losses, whereas the silver nanoparticles enhance the efficiency through surface plasmon resonance.[95] Similarly, Gunji *et al.* investigated a germanate glass layer

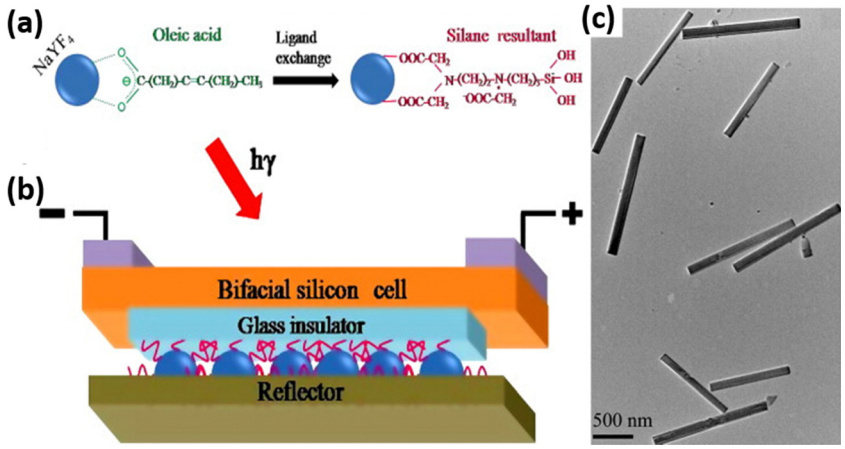

Fig. 19 (a) Ligand exchange of $NaYF_4$:Er nanocrystals. (b) A schematic of upconversion film application in silicon solar cells. (c) TEM image of $NaYF_4$:Er nanocrystals dispersed in methanol after ligand exchange. Reprinted with permission from Elsevier.[76]

doped with Eu^{3+} ions and TiO_2 nanoparticles.[97] The refractive index requirements for this kind of glass-based configuration were confirmed by Zampiva *et al.* who used a simulation approach. It was observed that different layered configurations having an increasing refractive index right from the air interface to the bottom layer of solar cells were most efficient in reducing the reflection losses. Also, they fabricated a forsterite-based thin film, which provided the additional benefit of scratch resistance, humidity control and enhanced stability for the solar cell.[97] The UCNPs showed an enhancement in the PCE of solar cells but the overall external quantum efficiency remained low.

To overcome this issue, Chen *et al.* investigated the role of the loading medium on the UCNP performance. They synthesized a transparent UC film *via* a silane ligand exchange reaction (shown in Fig. 19), which provided the additional properties of strong bonding with the glass substrate, hydrophilic behaviour and enhanced the emission intensity. At the same time, it reduced the effects of the luminescence quenching of bare C–H and C–C vibrational oscillators. The low IR radiation screening capability of this rigid ligand exchange thereby resulted in an overall efficiency enhancement from 7.68% to 8.337% for a bifacial silicon solar cell. A transparent UC film could be utilised for further applications in the development of transparent solar cells.[76] Similarly, the upconverter could be placed at the backside of the solar cell along with a reflective coating in which the upconverted light will get reflected to the silicon solar cell. However, the fabrication of the upconversion layer within the solar cell device remains a superior alternative to eliminate the reflection losses present in the glass-based fabrication strategy and removes the additional requirement of the matching oil. An alternate strategy is to use UCNPs on the backside of the solar cells.

This has been explored by Ho *et al.* who utilised a YF_3 matrix doped with Yb^{3+}/Er^{3+} on the backside of silicon solar cells, since theoretically, the NIR-IR region of light could pass through a 150-μm-thick silicon substrate. These UCNPs were mixed with SiO_2 at different concentrations of 3, 10, 20 and

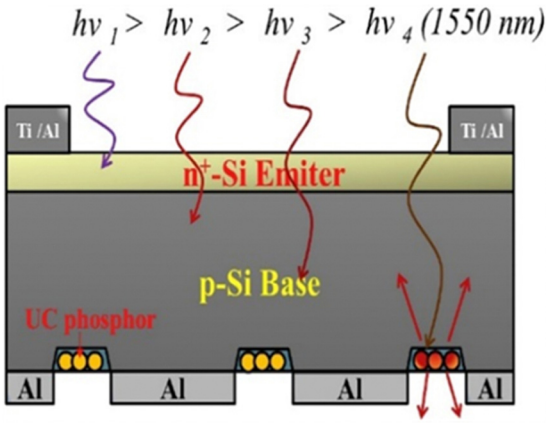

Fig. 20 A schematic diagram showing a silicon solar cell with SiO_2 coating containing YF_3:Yb^{3+}/Er^{3+} phosphor particles within the backside matrix grooves for use in the upconversion of photons under excitation by a light source with a wavelength of 1550 nm. Reprinted with permission from Elsevier.[77]

30 wt%. Here, SiO_2 also served as a passivation layer that additionally improved the solar cell efficiency. An array of groves (shown in Fig. 20) was formed using photolithographic etching and upconversion material was deposited in the as-designed groves. This setup yielded an increase in efficiency from 7.55% to 8.55% at a 30 wt% concentration of UCNP.[77] The same group also investigated a similar device but with further improvements, including the texturization of silicon and Al_2O_3 as a passivation layer. The Al_2O_3 was further doped with Er/Yb nanophosphor to combine the effects of the passivation layer with upconversion. They also studied the effect of using silver as an anti-reflection coating at the back of the solar cell. The solar cell with 3 layers of SiO_2 mixed with UNCP along with Al_2O_3 and silver coating yielded an efficiency enhancement of 3.84%.[98] On the other hand, Wild *et al.* studied the effect of $NaYF_4$:$Yb^{3+}{}_{18\%}/Er^{3+}{}_{2\%}$ on the performance of amorphous silicon solar cells in combination with white paint back-reflectors. The UCNPs were dissolved in a solution of PMMA

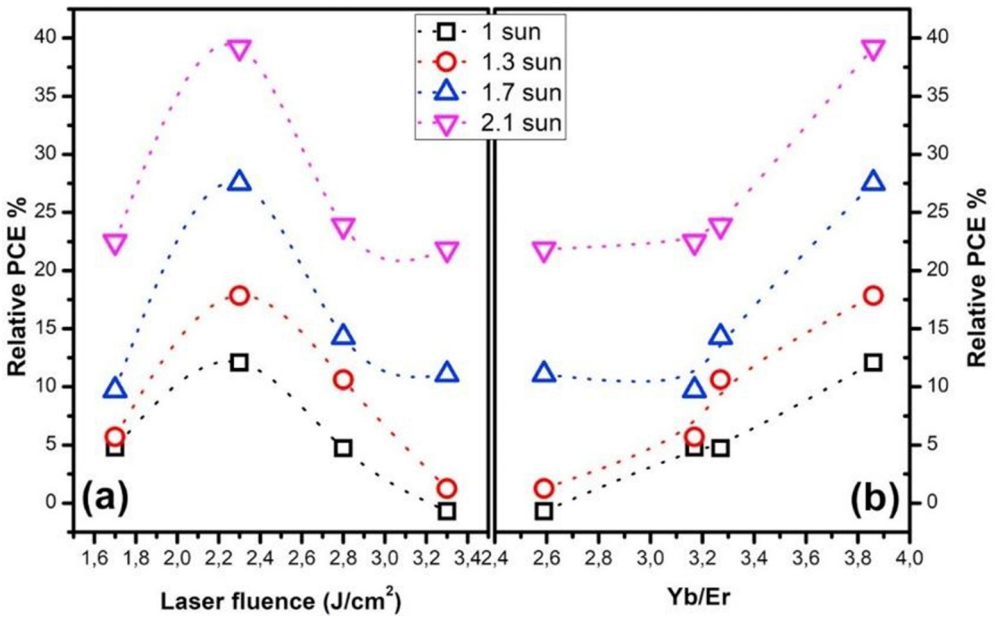

Fig. 21 The relative PCE dependence on the laser fluence (a), and (b) the Yb/Er elemental ratio measured at different solar simulator incident powers. Reprinted with permission from Elsevier.[75]

that was spin-coated on the backside of the standard p–i–n amorphous Si solar cell, which enhanced the short-circuit current density of 5 μA cm^{-2} using a 4 mW laser light.[99] An important question that needs to be addressed while discussing these techniques is the adhesive properties of these nanoparticles on silicon substrates to get good-quality films. Trabelsi *et al.* utilised the spin coating technique for the thin film deposition of TiO_2:Er^{3+}–Yb^{3+}. They investigated the SEM images to determine the adhesion properties of these UCNPs. It was found that the UCNPs adhered firmly to the n-Si substrate and formed a uniform thin layer.[100] This backside configuration turned out to be an easy, yet efficient way of incorporating UCNPs into the devices, but drop-casting and spin-coating techniques still give films in the micrometre range, and there is still non-uniformity.

For further fabrication of controllable and uniform conformal thin films, other techniques need to be adopted. Grigoroscutta *et al.* investigated the CeO_2 UC film doped with Yb/Er on a silicon solar cell prepared through pulsed laser deposition (PLD). The film was found to be affected by the PLD laser fluence, which varied from 1.7 J cm^{-2} to 3.7 J cm^{-2}. The host matrix, CeO_2 or ceria, has a phonon energy of 465 cm^{-1} and is transparent to the UV-Visible-NIR spectrum. Additionally, it has a greater capacity for the isomorphous substitution of rare earth ions. The solar cell characteristics for the p^+–n–n^+ Si diode were studied before and after CeO_2 film deposition. It was observed that the different morphologies of CeO_2 film (columnar, island and pyramidal) varied with the laser fluence. The film with the highest out-of-plane growth with respect to the in-plane growth component gave rise to an equiaxial spherical morphology and the highest device performance enhancement. While there was enhanced emission intensity with the increase in film thickness, growth defects also increased, which acted as luminescence quenchers. Therefore, the thickness of the film also affects the upconversion efficiency. The PCE varied with the laser fluence of PLD (shown in Fig. 21) and with the dopant (Yb/Er) elemental composition. It was found that the maximum efficiency of the solar cell was obtained at an elemental ratio of Yb : Er close to 4 and using film grown at 2.3 J cm^{-2} PLD laser fluence. A relative external quantum efficiency of 8.2% was obtained along with a maximum relative photoconversion efficiency of 12.1% for one-sun illumination.[79] Ghazy *et al.* utilised the atomic layer deposition technique for the thin film deposition of $(Er,Ho)_2O_3$. They fabricated films with different thicknesses where the film with the highest thickness, *i.e.*, 60 nm, gave the highest efficiency enhancement.[101] Thus, deposition techniques are an important variable for the development of upconversion-based photovoltaics.

The effects of surface plasmon resonance enhancement on upconversion luminescence have also been studied for silicon solar cells. Li *et al.* studied the efficiency enhancement in a p–i–n hydrogenated amorphous silicon solar cell using $NaYF_4$:Yb/Er/Gd nanorods combined with gold nanoparticles. The UCNPs could be tuned in size up to 10 nm, with a cubic or hexagonal phase, and blue to green emission colour, using different doping concentrations. The UCNPs exhibited two strong emission bands at 540 and 660 nm, and a weak emission peak at 524 nm, corresponding to the $^4S_{3/2} \rightarrow {}^4I_{15/2}$, $^4F_{9/2} \rightarrow {}^4I_{15/2}$ and $^2H_{11/2} \rightarrow {}^4I_{15/2}$ transitions of Er^{3+}, respectively. However, the formation of the nanorod architecture combined with gold nanoparticles improved the emission intensity by a factor of 3.2 and 9.6, respectively. A comparative study of the effects of the Au shell and nanoparticles on emission intensity

Table 2 Summary of the discussed solar cells

Device	UCNP	V_{oc}	J_{sc} (mA cm^{-2})	PCE (without UNCP)	PCE (with UNCP)	Enhancement (%)	Year/ref.
DSSC	YbF_3/Ho^{3+}	0.71	18.58	6.5	8.0	23	2016[58]
DSSC	$NaGdF_4$:Yb,Er	0.785	12.62	5.8	7.04	21.3	2013[59]
DSSC	Y_2O_3/Yb^{3+},Ho^{3+}	0.791	18.97	8.9	9.82	10.33	2020[60]
DSSC	CeO_2/Er^{3+},Yb^{3+}	0.62	14.46	5.65	6.12	8.31	2022[61]
DSSC	$BiYO_3/Er^{3+}$,Yb^{3+}	0.701	16.78	5.73	6.2	8.2	2021[62]
DSSC	$NaYF_4$:Yb,Er@$NaGdF_4$:Nd@SiO_2	0.74	14.26	5.13	6.65	29.63	2022[63]
DSSC	$NaYF_4:Er^{3+}$,Yb^{3+}@SiO_2	0.71	13.03	5.96	6.34	6.3	2013[64]
DSSC	$NaYF_4:Yb^{3+}$,Er^{3+}@$NaYF_4:Nd^{3+}$ core			7.573	8.658	13.1	2017[65]
DSSC	$NaYF_4:Yb^{3+}$,Er^{3+}@$NaYF_4:Eu^{3+}$ core/shell	0.764	14.3	6.726	7.664	13.9	2018[87]
DSSC	$NaYF_4:Yb^{3+}/Er^{3+}$@YOF:Yb^{3+}/Er^{3+} core/shell	0.74	16.53	7.02	8.39	17.1	2017[88]
Commercial Si solar cell	Fluoroindate glass/Er^{3+},Yb^{3+}	—	—	—	—	0.1	2013[75]
p–i–n amorphous Si	$NaYF_4:Er^{3+}Yb^{3+}$	—	10^{-5}	—	—	—	2010[99]
Bifacial silicon	$NaYF_4:Er^{3+}$	0.596	36.861	7.68	8.337	8.6	2012[76]
p^+–n–n^+ Si diode	$CeO_2:Yb^{3+}$,Er^{3+}	—	3.7	—	—	12.1	2018[79]
Hydrogenated amorphous Si	$NaYF_4$:Yb/Er/Gd with Au nanoparticles	0.41	1.16	—	—	—	2011[80]
Commercial crystalline Si solar cell	$SiO_2:YF_3:Er^{3+}$,Yb^{3+}	0.516	23.91	7.55	8.55	13.26	2019[93]
Al/textured Si/SiN_x/Ag	$SiO_2/Al_2O_3:Er^{3+}$,Yb^{3+}	0.604	40.99	16.91	17.56	3.84	2021[98]
FTO/TiO_2/UCNP/$MAPbI_3$/spiro-oMeTAD/Au	$LiYF_4:Er^{3+}$,Yb^{3+}	1.0	21	11	11.869	7.9	2016[66]
FTO/TiO_2 nanorods + UCNP/$MAPbI_3$/spiro-oMeTAD/Ag	TiO_2 nanorods: Er^{3+}	0.67	22.97	9.1	10.6	16.5	2018[67]
FTO/TiO_2/$MAPbI_3$/UCNP/spiro-oMeTAD/Ag	$NaYF_4:Er^{3+}$,Yb^{3+}	1.04	20.48	13.32	15.17	13.38	2018[92]
FTO/TiO_2 nanorods/$MAPbI_3$/spiro-oMeTAD + UCNP/Ag	$Li(Gd,Y)F_4:Yb^{3+}$,Er^{3+}	1.1	23.14	14.69	18.34	24.8	2019[68]
FTO/TiO_2/ZrO_2:UCNP/perovskite/carbon	$NaYbF_4:Ho^{3+}$	0.975	25.16	11.12	14.32	28.8	2018[69]
FTO/TiO_2 nanorods/SiO_2:UCNP:SiO_2/ perovskite/carbon	$SiO_2/NaYF_4:Yb^{3+}$,Er^{3+}@ SiO_2 core–shell	1.019	21.27	11.87	14.01	18	2019[71]
ITO/SnO_2/perovskite/UCNP/spiro- oMeTAD + UCNP/Au	$NaGdF_4:Er^{3+}/Yb^{3+}$	1.063	24.6	18.01	21.1	14.6	2022[70]
FTO/perovskite/spiro-OMeTAD/UCNPs/Au	$NaYF_4:Yb^{3+}$,Er^{3+}	1.07	21.67	13.61	15.56	8.4	2019[89]
FTO/c-TiO_2/UCNPs/perovskite/ UCNPs/spiro-OMeTAD/Au	$NaYF_4:Yb^{3+}$,Tm^{3+}	1.06	25.46	15.2	18.2	19.7	2019[72]
ITO/SnO_2/perovskite/UCNPs/ spiro-OMeTAD + UCNPs/Au	$NaCsWO_3$@$NaYF_4$@$NaYF_4:Yb^{3+}$,Er^{3+}	1.08	23.26	17.99	18.89	5	2021[93]
ITO/SnO_2/Au nanorods/UCNP + IR-783/perovskite/spiro-OMeTAD/Au	$NaYF_4:Yb_{3+}$,Er^{3+}@$NaYF_4:Yb^{3+}$,Nd^{3+} core–shell	1.167	23.26	19.4	21.1	8	2020[74]

was also conducted, which demonstrated a better efficiency using Au nanoparticles with UCNP. The solar cell with UCNP and Au nanoparticles showed a maximum efficiency enhancement of 72 times with a short-circuit current of 1.16 mA.[80] Thakur *et al.* synthesized a composite of graphene with SiO_2-coated UCNP. Here, the UCNPs were exploited as photoabsorbers and graphene acted as the electron transport layer. They fabricated a highly responsive photodetector giving a photoresponsivity of 2.7×10^4 A W^{-1} as compared to the initial 1.52×10^4 A W^{-1} under a 1.0 V bias and 980 nm irradiation. This approach could be utilised for efficiency enhancement in Si-graphene-based photovoltaics.[102]

Although upconversion materials have been integrated into silicon solar cells, their potential has not yet been fully exploited and the growth of UCNP thin films remains a barrier to their practical application in various deposition techniques. The integration of UCNPs into the active layers of silicon solar cells is, therefore, necessary for the effective improvement of photovoltaic performance.

4. Conclusion and outlook

This review highlights the various mechanisms of the upconversion process and their applications in different photovoltaic technologies, including silicon, perovskite, and dye-sensitized solar cells (summarised in Table 2). The recent advancements in this strategy of enhancing the performance of solar cells are being widely explored. Several upconversion materials have been developed, of which the most promising matrix is $NaYF_4$ due to its low phonon energy and activation by heavier lanthanide dopant ions like Yb^{3+}, Er^{3+} and Eu^{3+}, *etc.*, leading to high efficiency along with high absorption cross-section area and narrow crystal field splitting. These matrices help to cover the broader range of the solar spectrum that often goes wasted by the present technologies of photovoltaics. They not only increase the light-harvesting efficiency of the solar cell but they are also beneficial for various other issues in current solar technology, including the presence of pinholes, losses due to surface charge recombination, and the roughness of deposited films (shown in Fig. 22). Therefore, the host matrix with maximum power conversion efficiency needs to be explored.

The efficiency of these architectures can further be enhanced using various strategies, including the formation of core–shell architectures, dye sensitization, and surface plasmon resonance as discussed in the previous sections. Additionally, upconversion nanoparticles are known to enhance the internal multiple scattering-mediated absorption of light that improves the light-harvesting capability of the various devices. The dye-sensitized solar cells and perovskite solar cells have shown tremendous results in efficiency with the incorporation of upconversion nanoparticles. The long battle of the stability issues of perovskite solar cells has been addressed using upconversion films to a certain extent. Many efficiency-enhancement strategies, including dye sensitization of the upconversion matrix, have been incorporated; however, the enhancement due to upconversion remains low. In the case of dye sensitization, the functionality of the dye determines the binding ability of the dye with the nanoparticles. Thus, the effect of different functionalities on the upconversion efficiency needs to be investigated. Along with this, surface plasmon resonance phenomena with different types of nanoparticles could be explored thoroughly to achieve better upconversion performance.

Silicon solar cells are the traditional pioneers of the photovoltaic industry and are near their theoretical efficiency limit and, thereby, various strategies have been recently adopted to tune their performance. However, most strategies include the use of upconversion nanoparticles on glass substrates, which are assembled along with the solar cell. A much better way would be to incorporate the matrix into various layers of the solar cells to minimize the reflection losses. In addition, the use of a matching oil interface between the solar cell and

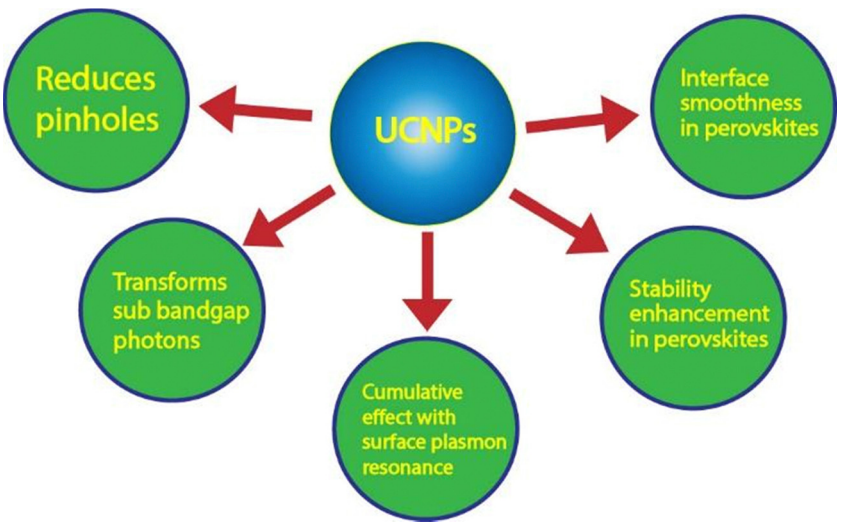

Fig. 22 The overall effects of upconversion nanoparticles on different solar cells.

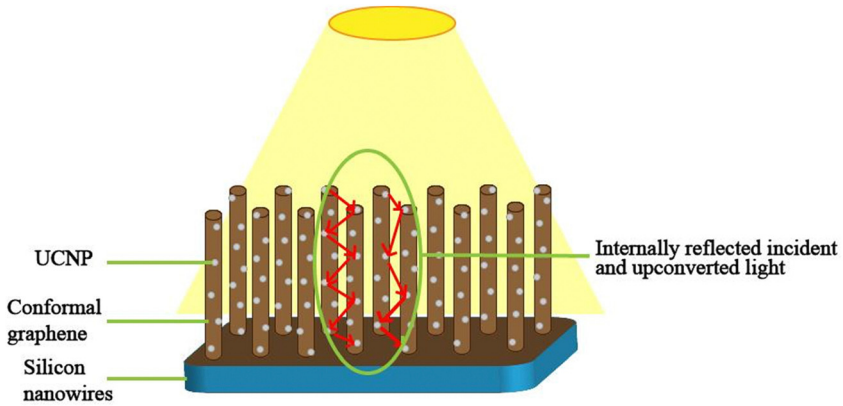

Fig. 23 Schematic of the proposed solar cell with conformally coated graphene on silicon nanowires coated with upconversion nanoparticles.

glass-based upconversion strategy poses various challenges when used along with textured solar cells including silicon nanowire-based technology and graphene-based silicon solar cells deteriorating the graphitic layer. Therefore, alternate strategies of device fabrication, including deposition techniques like sputtering, pulse layer deposition and atomic layer deposition, should be further explored. One such device fabrication strategy could be to use silicon nanowire architecture conformally coated with graphene and decorated with UCNPs (as shown in Fig. 23). Here, the UCNPs would transform the sub-bandgap photons and the upconverted light would be internally reflected and absorbed on the nanowire surface, which has been demonstrated in photovoltaic as well as photoelectrochemical applications.[103,104] This configuration would eliminate the need for reflector materials to transfer upconverted light at the junction of the solar cell. Upconversion materials have potential applications in solving the energy demands of the world. Despite the various benefits of upconversion, the cost of lanthanides and upconversion photoluminescence efficiency need further exploration for the advancement of the photovoltaic industry and increasing renewable energy applications.

Conflicts of interest

There are no conflicts to declare.

Acknowledgements

K. G. is grateful to Ministry of Textiles [Grant 2/3/2021-NTTM(Pt.)], Govt. of India. N. C. is thankful to CSIR, New Delhi, India [Grant No.-09/1129(13373)/2022-EMR-I] for providing financial support.

References

1 Solar Energy, IRENA, https://www.irena.org/Energy-Transition/Technology/Solarenergy.
2 World Energy Resources: Solar,World Energy Council 2013, https://www.worldenergy.org/assets/images/imported/2013/10/WER_2013_8_Solar_revised.pdf.
3 C. Chen, S. Zheng and H. Song, *Chem. Soc. Rev.*, 2021, **50**, 7250–7329.
4 The History of Solar, https://www1.eere.energy.gov/solar/pdfs/solar_timeline.pdf.
5 Solar Energy Market Outlook. 2026, https://www.alliedmarketresearch.com/solar-energymarket.
6 IEA (2022), Solar PV, IEA, Paris, https://www.iea.org/reports/solar-pv.
7 Operation and Physics of Photovoltaic Solar Cells: An Overview, https://revistas.utp.ac.pa.
8 C. Ballif, F.-J. Haug, M. Boccard, P. J. Verlinden and G. Hahn, *Nat. Rev. Mater.*, 2022, **7**, 597–616.
9 P. K. Nayak, S. Mahesh, H. J. Snaith and D. Cahen, *Nat. Rev. Mater.*, 2019, **4**, 269–285.
10 PV Magazine, https://www.pv-magazine.com/2022/11/21/longi-claims-worlds-highest-silicon-solar-cell-efficiency.
11 A. Ghazy, M. Safdar, M. Lastusaari, H. Savin and M. Karppinen, *Sol. Energy Mater. Sol. Cells*, 2021, **230**, 111234.
12 W. Shockley and H. J. Queisser, *J. Appl. Phys.*, 1961, **32**, 510–519.
13 C. Strümpel, M. McCann, G. Beaucarne, V. Arkhipov, A. Slaoui, V. Švrček, C. Del Cañizo and I. Tobias, *Sol. Energy Mater. Sol. Cells*, 2007, **91**, 238–249.
14 X. Liu, T. Chen, Y. Gong, C. Li, L. Niu, S. Xu, X. Xu, L. Pan, J. G. Shapter, Y. Yamauchi, J. Na and M. Eguchi, *J. Photochem. Photobiol., Part C*, 2021, **47**, 100404.
15 D. I. Kim, J. W. Lee, R. H. Jeong and J.-H. Boo, *Sci. Rep.*, 2022, **12**, 697.
16 A. S. Sharma, A. Pusch, M. P. Nielsen, U. Römer, M. J. Y. Tayebjee, F. E. Rougieux and N. J. Ekins-Daukes, *Sol. Energy*, 2022, **237**, 44–51.
17 N. S. Satpute, C. M. Mehare, A. Tiwari, H. C. Swart and S. J. Dhoble, *ACS Appl. Electron. Mater.*, 2022, **4**, 3354–3391.
18 A. Shalav, B. S. Richards and M. A. Green, *Sol. Energy Mater. Sol. Cells*, 2007, **91**, 829–842.
19 J. Chen and J. X. Zhao, *Sensors*, 2012, **12**, 2414–2435.

20 Y. Shang, S. Hao, C. Yang and G. Chen, *Nanomaterials*, 2015, **5**, 1782–1809.
21 B. Zhou, B. Shi, D. Jin and X. Liu, *Nat. Nanotechnol.*, 2015, **10**, 924–936.
22 B. Golesorkhi, H. Nozary, A. Fürstenberg and C. Piguet, *Mater. Horiz.*, 2020, **7**, 1279–1296.
23 H. Dong, L.-D. Sun and C.-H. Yan, *Nanoscale*, 2013, **5**, 5703.
24 B. Zhou, L. Yan, L. Tao, N. Song, M. Wu, T. Wang and Q. Zhang, *Adv. Sci.*, 2018, **5**, 1700667.
25 J. Huang, L. Yan, Z. An, H. Wei, C. Wang, Q. Zhang and B. Zhou, *Adv. Mater.*, 2023, 2310524.
26 F. Auzel, *Chem. Rev.*, 2004, **104**, 139–174.
27 J. F. Da Silva, R. F. Da Silva, E. P. Santos, L. J. Q. Maia and A. L. Moura, *Appl. Phys. Lett.*, 2020, **117**, 151102.
28 P. Bharmoria, H. Bildirir and K. Moth-Poulsen, *Chem. Soc. Rev.*, 2020, **49**, 6529–6554.
29 W. Yang, X. Li, D. Chi, H. Zhang and X. Liu, *Nanotechnology*, 2014, **25**, 482001.
30 S. Fischer, R. D. Mehlenbacher, A. Lay, C. Siefe, A. P. Alivisatos and J. A. Dionne, *Nano Lett.*, 2019, **19**, 3878–3885.
31 R. G. Felsted, A. Pant, A. B. Bard, X. Xia, D. R. Luntz-Martin, S. Dadras, S. Zhang, A. N. Vamivakas and P. J. Pauzauskie, *Cryst. Growth Des.*, 2022, **22**, 3605–3612.
32 X. Zhang, M. Wang, J. Ding, X. Song, J. Liu, J. Shao and Y. Li, *RSC Adv.*, 2014, **4**, 40223–40231.
33 X. Zhou, B. E. Smith, P. B. Roder and P. J. Pauzauskie, *Adv. Mater.*, 2016, **28**, 8658–8662.
34 S. P. Tiwari, S. K. Maurya, R. S. Yadav, A. Kumar, V. Kumar, M.-F. Joubert and H. C. Swart, *J. Vac. Sci. Technol., B: Nanotechnol. Microelectron.: Mater., Process., Meas., Phenom.*, 2018, **36**, 060801.
35 G. Wang, Q. Peng and Y. Li, *J. Am. Chem. Soc.*, 2009, **131**, 14200–14201.
36 R. Singh, E. Madirov, D. Busko, I. M. Hossain, V. A. Konyushkin, A. N. Nakladov, S. V. Kuznetsov, A. Farooq, S. Gharibzadeh, U. W. Paetzold, B. S. Richards and A. Turshatov, *ACS Appl. Mater. Interfaces*, 2021, **13**, 54874–54883.
37 X. He and B. Yan, *J. Mater. Chem. C*, 2013, **1**, 3910.
38 M. Haase and H. Schäfer, *Angew. Chem., Int. Ed.*, 2011, **50**, 5808–5829.
39 W. Kong, J. Shan and Y. Ju, *Mater. Lett.*, 2010, **64**, 688–691.
40 L.-Y. Yang, Y.-J. Dong, D.-P. Chen, C. Wang, N. Da, X. Jiang, C. Zhu and J. Qiu, *Opt. Express*, 2005, **13**, 7893.
41 S. R. Johannsen, L. R. Lauridsen, B. Julsgaard, P. T. Neuvonen, S. K. Ram and A. N. Larsen, *Thin Solid Films*, 2014, **550**, 499–503.
42 C. Xu, Q. Yang, G. Ren and Y. Liu, *J. Alloys Compd.*, 2010, **503**, 82–85.
43 B. S. Cao, J. L. Wu, N. S. Yu, Z. Q. Feng and B. Dong, *Thin Solid Films*, 2014, **550**, 495–498.
44 R. L. Tranquilin, L. X. Lovisa, C. R. R. Almeida, C. A. Paskocimas, M. S. Li, M. C. Oliveira, L. Gracia, J. Andres, E. Longo, F. V. Motta and M. R. D. Bomio, *J. Phys. Chem. C*, 2019, **123**, 18536–18550.
45 N. R. Aghamalyan, G. G. Demirkhanyan, R. K. Hovsepyan, R. B. Kostanyan and D. G. Zargaryan, *Opt. Mater.*, 2010, **32**, 1046–1049.
46 M. Yang, Y. Liang, Q. Gui, B. Zhao, D. Jin, M. Lin, L. Yan, H. You, L. Dai and Y. Liu, *Sci. Rep.*, 2015, **5**, 11844.
47 J. L. Wu, B. S. Cao, F. Lin, B. J. Chen, J. S. Sun and B. Dong, *Ceram. Int.*, 2016, **42**, 18666–18673.
48 R. Naccache, Q. Yu and J. A. Capobianco, *Adv. Opt. Mater.*, 2015, **3**, 482–509.
49 K. Du, J. Feng, X. Gao and H. Zhang, *Light: Sci. Appl.*, 2022, **11**, 222.
50 A. Nadort, J. Zhao and E. M. Goldys, *Nanoscale*, 2016, **8**, 13099–13130.
51 K. Malhotra, D. Hrovat, B. Kumar, G. Qu, J. V. Houten, R. Ahmed, P. A. E. Piunno, P. T. Gunning and U. J. Krull, *ACS Appl. Mater. Interfaces*, 2023, **15**, 2499–2528.
52 H. Liu, K. Huang, R. R. Valiev, Q. Zhan, Y. Zhang and H. Ågren, *Laser Photonics Rev.*, 2018, **12**, 1700144.
53 S. Han, R. Deng, X. Xie and X. Liu, *Angew. Chem., Int. Ed.*, 2014, **53**, 11702–11715.
54 X. Zheng, Y. Chen, S. Pan, Z. Liu, D. Xu, Y. Zhang and H. Lin, *J. Fluoresc. Chem.*, 2022, **261–262**, 110013.
55 R. K. Sharma, A.-V. Mudring and P. Ghosh, *J. Lumin.*, 2017, **189**, 44–63.
56 J. Hu, B. Zhao, R. Wen, X. Zhang, Y. Zhang, D. S. Kohane and Q. Liu, *Nano Lett.*, 2023, **23**, 5209–5216.
57 S. SeethaLekshmi, A. R. Ramya, M. L. P. Reddy and S. Varughese, *J. Photochem. Photobiol., Part C*, 2017, **33**, 109–131.
58 J. Yu, Y. Yang, R. Fan, P. Wang and Y. Dong, *Nanoscale*, 2016, **8**, 4173–4180.
59 P. Ramasamy and J. Kim, *Chem. Commun.*, 2014, **50**, 879–881.
60 P. Tadge, R. S. Yadav, P. K. Vishwakarma, S. B. Rai, T.-M. Chen, S. Sapra and S. Ray, *J. Alloys Compd.*, 2020, **821**, 153230.
61 M. Ambapuram, M. M. Parnapalli, G. Maddala, V. Tankasala, S. Kalvapalli and R. Mitty, *Opt. Mater.*, 2022, **129**, 112515.
62 J. Dutta and V. K. Rai, *Opt. Laser Technol.*, 2021, **140**, 107087.
63 S. Zhang, S. Dun, X. Guo and J. Zhang, *Electrochim. Acta*, 2022, **421**, 140435.
64 Z. Zhou, J. Wang, F. Nan, C. Bu, Z. Yu, W. Liu, S. Guo, H. Hu and X.-Z. Zhao, *Nanoscale*, 2014, **6**, 2052–2055.
65 S. Hao, Y. Shang, D. Li, H. Ågren, C. Yang and G. Chen, *Nanoscale*, 2017, **9**, 6711–6715.
66 X. Chen, W. Xu, H. Song, C. Chen, H. Xia, Y. Zhu, D. Zhou, S. Cui, Q. Dai and J. Zhang, *ACS Appl. Mater. Interfaces*, 2016, **8**, 9071–9079.
67 H. Zhang, Q. Zhang, Y. Lv, C. Yang, H. Chen and X. Zhou, *Mater. Res. Bull.*, 2018, **106**, 346–352.
68 X. Deng, C. Zhang, J. Zheng, X. Zhou, M. Yu, X. Chen and S. Huang, *Appl. Surf. Sci.*, 2019, **485**, 332–341.
69 Y. Li, L. Zhao, M. Xiao, Y. Huang, B. Dong, Z. Xu, L. Wan, W. Li and S. Wang, *Nanoscale*, 2018, **10**, 22003–22011.

70 J. Wu, S. Wei, X. Weng, R. Wang, H. Zhou and S. Cheng, *Sol. Energy Mater. Sol. Cells*, 2022, **248**, 112029.
71 F. Qi, Y. Xiao, Z. Yu, P. Liu, S. Kong, F. Li, H. Zhang, Y. Wang and X.-Z. Zhao, *Org. Electron.*, 2019, **73**, 152–158.
72 D. Ma, Y. Shen, T. Su, J. Zhao, N. U. Rahman, Z. Xie, F. Shi, S. Zheng, Y. Zhang and Z. Chi, *Mater. Chem. Front.*, 2019, **3**, 2058–2065.
73 M. Xu, Z. Xu, Z. Sun, W. Chen, L. Wang, Y. Liu, Y. Wang, X. Du and S. Pan, *ACS Appl. Mater. Interfaces*, 2023, **15**, 3664–3672.
74 W. Bi, Y. Wu, C. Chen, D. Zhou, Z. Song, D. Li, G. Chen, Q. Dai, Y. Zhu and H. Song, *ACS Appl. Mater. Interfaces*, 2020, **12**, 24737–24746.
75 M. A. Hernández-Rodríguez, M. H. Imanieh, L. L. Martín and I. R. Martín, *Sol. Energy Mater. Sol. Cells*, 2013, **116**, 171–175.
76 S. Chen, G. Zhou, F. Su, H. Zhang, L. Wang, M. Wu, M. Chen, L. Pan and S. Wang, *Mater. Lett.*, 2012, **77**, 17–20.
77 W.-J. Ho, C.-Y. Wei, J.-J. Liu, W.-C. Lin and C.-H. Ho, *Vacuum*, 2019, **166**, 1–5.
78 W. Ho, P. Lu and J. Liu, *Int. J. Energy Res.*, 2022, **46**, 278–289.
79 M. Grigoroscuta, M. Secu, L. Trupina, M. Enculescu, C. Besleaga, I. Pintilie and P. Badica, *Sol. Energy*, 2018, **171**, 40–46.
80 Z. Q. Li, X. D. Li, Q. Q. Liu, X. H. Chen, Z. Sun, C. Liu, X. J. Ye and S. M. Huang, *Nanotechnology*, 2012, **23**, 025402.
81 B. O'Regan and M. Grätzel, *Nature*, 1991, **353**, 737–740.
82 T. W. Hamann, R. A. Jensen, A. B. F. Martinson, H. Van Ryswyk and J. T. Hupp, *Energy Environ. Sci.*, 2008, **1**, 66.
83 M. Kokkonen, P. Talebi, J. Zhou, S. Asgari, S. A. Soomro, F. Elsehrawy, J. Halme, S. Ahmad, A. Hagfeldt and S. G. Hashmi, *J. Mater. Chem. A*, 2021, **9**, 10527–10545.
84 A. A. Ansari, V. K. Thakur and G. Chen, *Coord. Chem. Rev.*, 2021, **436**, 213821.
85 K. Kim, S. K. Nam and J. H. Moon, *ACS Appl. Energy Mater.*, 2020, **3**, 5277–5284.
86 G. Shan and G. P. Demopoulos, *Adv. Mater.*, 2010, **22**, 4373–4377.
87 T. Chen, Y. Shang, S. Hao, L. Tian, Y. Hou and C. Yang, *Electrochim. Acta*, 2018, **282**, 743–749.
88 L. Tian, Y. Shang, S. Hao, Q. Han, T. Chen, W. Lv and C. Yang, *Adv. Funct. Mater.*, 2018, **28**, 1803946.
89 J. Park, K. Kim, E.-J. Jo, W. Kim, H. Kim, R. Lee, J. Y. Lee, J. Y. Jo, M.-G. Kim and G. Y. Jung, *Nanoscale*, 2019, **11**, 22813–22819.
90 S. S. Dipta and A. Uddin, *Energy Technol.*, 2021, **9**, 2100560.
91 C. Chen, S. Zheng and H. Song, *Chem. Soc. Rev.*, 2021, **50**, 7250–7329.
92 L. Qiu, Y. Yang, G. Dong, D. Xia, M. Li, X. Fan and R. Fan, *Appl. Surf. Sci.*, 2018, **448**, 145–153.
93 F. Xu, Y. Sun, H. Gao, S. Jin, Z. Zhang, H. Zhang, G. Pan, M. Kang, X. Ma and Y. Mao, *ACS Appl. Mater. Interfaces*, 2021, **13**, 2674–2684.
94 C. Battaglia, A. Cuevas and S. De Wolf, *Energy Environ. Sci.*, 2016, **9**, 1552–1576.
95 J. A. M. Garcia, L. Bontempo, L. A. Gomez-Malagon and L. R. P. Kassab, *Opt. Mater.*, 2019, **88**, 155–160.
96 C. Fuentes-Hernandez, W.-F. Chou, T. M. Khan, L. Diniz, J. Lukens, F. A. Larrain, V. A. Rodriguez-Toro and B. Kippelen, *Science*, 2020, **370**, 698–701.
97 R. Y. S. Zampiva, C. G. Kaufmann, L. H. Acauan, R. L. Seeger, F. Bonatto, C. D. Boeira, W. Q. Santos, C. Jacinto, C. A. Figueroa, L. S. Dorneles, A. K. Alves, C. P. Bergmann and C. S. Ten Caten, *Sol. Energy*, 2018, **170**, 752–761.
98 W. Ho, P. Lu and J. Liu, *Int. J. Energy Res.*, 2022, **46**, 278–289.
99 J. De Wild, A. Meijerink, J. K. Rath, W. G. J. H. M. Van Sark and R. E. I. Schropp, *Sol. Energy Mater. Sol. Cells*, 2010, **94**, 1919–1922.
100 F. Trabelsi, F. Mercier, E. Blanquet, A. Crisci and R. Salhi, *Ceram. Int.*, 2020, **46**, 28183–28192.
101 A. Ghazy, M. Safdar, M. Lastusaari, A. Aho, A. Tukiainen, H. Savin, M. Guina and M. Karppinen, *Sol. Energy Mater. Sol. Cells*, 2021, **219**, 110787.
102 M. K. Thakur, A. Gupta, M. Y. Fakhri, R. S. Chen, C. T. Wu, K. H. Lin and S. Chattopadhyay, *Nanoscale*, 2019, **11**, 9716–9725.
103 S. Riyajuddin, S. Kumar, D. Badhwar, S. A. Siddiqui, J. Sultana and K. Ghosh, *Sustainable Energy Fuels*, 2021, **5**, 3160–3171.
104 S. Riyajuddin, J. Sultana, S. A. Siddiqui, S. Kumar, D. Badhwar, S. S. Yadav, S. Goyal, A. Venkatesan, S. Chakraverty and K. Ghosh, *Sustainable Energy Fuels*, 2022, **6**, 197–208.